1991

P.W. Hemker, B. Koren

Efficient multi-dimensional upwinding for the steady Euler equations

CWI, nationaal instituut voor onderzoek op het gebied van wiskunde en informatica

Efficient Multi-Dimensional Upwinding for the Steady Euler Equations

P.W. Hemker, B. Koren
Centre for Mathematics and Computer Science
P.O. Box 4079, 1009 AB Amsterdam, The Netherlands

Abstract

Multi-dimensional upwind discretizations for the steady Euler equations are studied, with the emphasis on both a good accuracy and a good efficiency. The multi-dimensional upwind methods consist of a one-dimensional Riemann solver with a locally rotated left and right cell face state, the rotation angle depending on the local flow solution. On the basis of a model equation, we make first a study of the accuracy and stability properties of some of these multi-dimensional upwind schemes. One novel multi-dimensional scheme is derived for which smoothing analysis of point Gauss-Seidel relaxation shows that despite its rather low numerical diffusion, it still enables a good acceleration by multigrid. Another novel multi-dimensional scheme is derived which has no numerical diffusion in crosswind direction, and of which convergence analysis shows that its corresponding discretized equations can be solved efficiently by means of defect correction iteration with in the inner multigrid iteration the former multi-dimensional scheme. It is shown that for Euler flows, an appropriate local rotation angle can be found by maximizing a Riemann invariant along the middle subpath of the wave path in state space. For the steady, two-dimensional Euler equations, numerical results are presented for some supersonic test cases with an oblique contact discontinuity and for some supersonic test cases with an oblique shock wave. The numerical results are in good agreement with the theoretical predictions. Comparisons are made with results obtained by standard one-dimensional upwind schemes. The multi-dimensional results obtained compare very well, both with respect to accuracy and efficiency.

1 Introduction

1.1 Grid-coupled 1-D upwind schemes

Many upwind schemes used in multi-dimensional (multi-D) flow computations are based on the application of some one-dimensional (1-D) shock capturing scheme in a grid-aligned manner. Despite the rigorous mathematics involved in these 1-D upwind schemes, in most multi-D flow computations, the underlying 1-D upwind results are just superposed without rigorous mathematical justification. Besides this inconsistency in methodology, the grid-alignment (i.e. grid-dependency) is also inconsistent with the upwind principle that discretizations should be dependent on the solution only.

The above deficiencies are counterbalanced to a large extent by the advantage of simplicity in implementing the grid-aligned 1-D upwind approach. This simplicity holds in particular for finite volume discretizations, discretizations which are widely preferred for the Euler equations because of their trivial satisfaction of conservation properties and their discontinuous solution representation which allows discontinuities in the flow to be matched with the inter-volume discontinuities. (It is precisely this discontinuous solution representation which makes the finite volume implementation of the grid-aligned 1-D upwind approach so straightforward and simple.)

For many practical purposes, very satisfactory results are obtained by applying the grid-aligned 1-D upwind approach. However, sometimes the aforementioned flaws become clearly visible in the numerical results. For instance, the resolution of layers that are not aligned with the grid (and hence neither with the discretization) may be insufficient; oblique layers may be falsely diffused to an unacceptable extent. Changing from one shock capturing scheme to another (for instance from some flux splitting scheme to some flux difference splitting scheme) usually does not help in these cases. Simply lowering the magnitude of false diffusion by raising the order of accuracy of the underlying 1-D upwind scheme may help, but - possibly - at a very high increase in computational cost, because lowering the magnitude of false diffusion may significantly deteriorate the stability properties of the discretized equations. (In nonlinear practice, stability may even be lost.)

A proper balance needs to be found between both (multi-D) accuracy and stability. To achieve such a balance, one needs not just control false diffusion's magnitude, but - separately - both its magnitude and its direction. A way to control both separately, could be by introducing solution-adaptive grid rotation, maintaining for simplicity the grid-aligned 1-D upwind approach. However, for e.g. Euler flows (with their allowance for in principle any flow rotation), this may easily lead to undesirably complex grid rotations, rotations whose final control certainly re-introduces some sort of inconsistent grid-coupling into the discretization. From a viewpoint of consistency, accuracy and efficiency, it seems most natural to no longer ignore the multi-D nature of a multi-D flow in the upwind scheme itself. Unfortunately, despite the availability of fully developed 1-D upwind schemes, the development of a multi-D upwind scheme is not that straightforward; whereas in 1-D, solution layers can occur in one direction only, already in 2-D, solution layers can occur in infinitely many directions.

1.2 Grid-decoupled multi-D upwind schemes

Several grid-decoupled multi-D upwind discretizations have been published already and many more are still in development. Here we give a brief survey.

An approach which is widely applied and therefore should be mentioned first is that of initially ignoring any upwinding and just applying central differences (see e.g. [14]). Stability of the resulting system of unstably discretized equations may be obtained by adding positive artificial diffusion (i.e. by introducing some sort of artificial upwinding). Unfortunately, the proper amount of diffusion to be added is problem-dependent and not known in advance, which may lead to much trial and error, in particular when striving for a good multi-D accuracy. The same holds for about the opposite approach which is proposed in [36]. There, with a first-order, grid-aligned 1-D upwind scheme as the basic scheme, negative artificial diffusion is added explicitly for reasons of accuracy.

2

An early, principal upwind progress was made by Raithby, who made an accuracy analysis of upwinding applied to 2-D convection diffusion problems, with the convection at an angle to the grid lines [31]. Raithby found that a large error results in regions where the flow and grid lines are not closely aligned, and next proposed two skew upwind schemes which reduce this error [32]. Both schemes (automatically) detect the local flow angle and apply some specific upwinding in that direction. In [32], a substantial accuracy improvement is shown for both schemes, though still for scalar convection problems only.

Another early upwind progress was made by Moretti, who devised a characteristic-based upwind scheme for the unsteady multi-D Euler equations; the λ-scheme [25]. Unfortunately, the scheme is principally non-conservative. To avoid severe conservation errors at shock waves, there the non-conservative, characteristic-based relations need to be replaced by the Rankine-Hugoniot relations (shock fitting).

A conservative multi-D upwind scheme for the 2-D Euler equations was proposed by Davis [3]. To improve the resolution of oblique shock waves in a cell-centered finite volume discretization, Davis proposes to apply flux splitting in a rotated manner. Per cell face, Davis performs two flux computations: the first (normal to the possible shock wave crossing that cell face) with the flux splitting scheme in a first-order manner, the second (tangential to that possible shock wave) with any other suitable scheme (e.g. a central scheme). Combination of the two rotated fluxes determines the final flux across the cell face. (The ideas of applying a rotated discretization and distinct differences in one grid point - e.g. upwind in one specific direction and central in the direction normal to that - go back to Jameson [13] and Murman and Cole [26], respectively.) Though the rotated scheme proposed in [3] is only first-order accurate, the accuracy of the numerical results is quite impressive already. Of course, the price paid for it, when compared to grid-aligned 1-D flux splitting schemes (with one flux computation per cell face) is an increase in computational cost. By upwind differencing in one direction and central differencing in the normal direction, this increase is kept to a minimum, but unfortunately, another extra cost rises from the algorithm for detecting the shock angle. Besides its trivial cost for use, this algorithm may also spoil convergence. (In [3], the shock angle detection algorithm is based on local velocity gradients. Noise on these gradients may inhibit convergence.)

Whereas Davis confines himself to flux splitting (capturing oblique shock waves only), Baines [1] and Levy et al. [24] consider flux difference splitting (hence - in principle - capturing both oblique shock waves and oblique contact discontinuities). Further, in [24], non-Cartesian grids and higher-order accuracy are considered, and a simple weighted formula (a 'blended' formula) is proposed for detecting the angle of both oblique shock and shear waves. If at a cell face both waves seem to occur, the formula decides which of both waves is most dominant (and hence which wave can be resolved most accurately). The formula is based on a weighted average of the local pressure gradient and the local flow angle. An advantage of this formula is that it is rather resistant to wild, unwanted angle variations in nearly uniform flow regions. It cannot detect temperature contacts (i.e. contact discontinuities without any shear), but this can be easily repaired by also considering the temperature gradient. Unfortunately, no a-priori knowledge exists about the weights that should be given to the different gradients considered. A recent angle detection algorithm which is similar to that proposed in [24], in the sense that it takes into account the dominance of shock wave and shear wave when both occur at a cell face, is discussed in [34]. As opposed to the algorithm from [24], this algorithm does not require the tuning of a blended formula; a physically sound theory is presented for computing a dominant wave angle.

The problem of deciding between a shock wave or a shear wave does not exist for the ambitious multi-D upwind schemes which (try to) decompose the coupled system of unsteady Euler equations into a set of scalar, unsteady convection equations. Such decomposition methods have been proposed by Roe [33] and Hirsch et al. [11]. In these methods, more than one specific solution angle is associated with each cell face or grid point. (In the aforementioned rotated flux methods, there was only one such angle.) The method of Roe decomposes a 2-D Euler flow into five or six simple waves which propagate into directions which are determined from the local solution gradients. Hirsch et al. propose a local decoupling of the Euler equations, which is based on two characteristic directions. The two characteristic directions on their turn are based on local flow gradients. Complete Hirsch decoupling is not always possible. A nice property of the Hirsch decomposition compared to the Roe decomposition is its allowance for a more straightforward and efficient extension to 3-D. Applications of the Roe and Hirsch decompositions can be found already in [19, 28] and [12, 30, 37], respectively. Difficulties in applying both decompositions appear to be: satisfaction of the conservation properties (because decomposition leads to non-conservative equations) and sensitivity to noise (because of the dependence on flow gradients). Repairs for making the schemes conservative have been proposed already in the early papers [11, 33]. (The repair proposed in e.g. [11] consists of applying the grid-decoupled scheme in a predictor step and some conservative grid-coupled scheme in a corrector step.) So far, the remedies against noise are unsatisfactory; they simply consist of freezing the directions during the solution process.

Despite the large amount of theoretical work which has been put already in most of the aforementioned multi-D upwind schemes, so far it can be concluded that the quality of the numerical results is not yet quite satisfactory. Of course, much work in the further development of these schemes is still in progress.

1.3   Efficient solution methods

Though the emphasis in most multi-D upwind research clearly lies on a good accuracy, some work has also been directed already towards a good efficiency.

Examples in the context of explicit time stepping schemes are the work of LeVeque [23] and Catalano and Deconinck [2]. In [23] a technique is presented for improving the (multi-D) stability restriction on the time step. (Without this technique, the Cartesian grid approach followed in [23] leads to severe time step restrictions in the very small, sliced-off cells.) In [2], the aim is not just good stability, but also a good multi-D damping of high-frequency errors, the latter for the sake of a fruitful multigrid acceleration. For this purpose, for a 2-D advection equation, both the multi-D stability and the multi-D smoothing of a two-stage explicit time stepping scheme are optimized.

As far as we know, the only implicit solution methods for multi-D upwind discretizations are those proposed by Hirsch and Lacor [12], and Sidilkover [35]. Whereas Hirsch and Lacor consider unsteady flow equations, Sidilkover considers steady flow equations, and solves these directly (i.e. not through any unsteady form) by means of a multigrid method. A direct multigrid solution approach applied to steady, multi-D upwind discretizations is more ambitious than the direct approaches which have been developed for steady, 1-D upwind discretizations (see e.g. [5, 10, 15]); multi-D upwinding inherently leads to a greater sensitivity to noise and hence less robustness. Though Sidilkover does not show numerical results for real flow equations (such as e.g. the Euler equations), but confines himself to rather simple model equations, the numerical results presented in [35] are promising from a viewpoint of both accuracy and efficiency. They show that it is worthwhile to further investigate direct solution methods for multi-D upwind discretizations.

1.4 Present approach

Our aim is to develop for the steady Euler equations, in a cell-centered finite volume context: multi-D upwind methods with some optimal balance between multi-D accuracy and efficiency. The steady equations are solved directly (so not through an unsteady form). For good efficiency, we rely on nonlinear multigrid (multigrid-Newton) iteration. As the smoothing technique in the multigrid iteration, we apply point Gauss-Seidel relaxation, using the exact derivative matrices (exact Newton). The latter requires the cell face fluxes to be continuously differentiable. If for the multi-D schemes the multigrid solver does not directly meet our standards, we do not try to repair it, but - instead - we rely on defect correction iteration as an outer iteration, just as in [7, 16, 17]. The multi-D upwind schemes to be considered here are very simple schemes. They use neither decoupling of the Euler equations as in [11, 33], nor rotated fluxes as in [3, 24]. The schemes are based on *rotated left and right cell face states solely*. Per cell face, just as with grid-aligned 1-D upwind schemes, only a single numerical flux is computed: the one normal to the cell face. The only difference between grid-aligned 1-D upwind schemes and the present multi-D upwind schemes is that whereas in the first schemes the left and right cell face states are computed from a *solution-independent, 1-D* subset of the local multi-D solution, in the present multi-D upwind schemes, these states are computed from a *solution-dependent, multi-D* subset. The numerical flux function to be applied should allow a good resolution of both oblique shock waves and oblique contact discontinuities, which makes flux difference splitting schemes to be preferred above flux splitting schemes. Given the good experience with Osher's scheme [27] in combination with nonlinear multigrid [10], we apply this flux difference splitting scheme. The multi-D upwind schemes are analyzed (for accuracy and efficiency) on the basis of a 2-D, linear scalar model equation, discretized on a square, cell-centered finite volume grid. A property kept in mind is that novel schemes can be carried over to 3-D, and also that extension to non-Cartesian grids is possible.

The contents of the paper is as follows. To set a frame of reference, in section 2, accuracy analyses and also some simple stability analyses are performed for existing grid-aligned 1-D upwind schemes. Next, in section 3, some existing multi-D upwind schemes are analyzed and two novel schemes are derived, still mainly from the viewpoint of accuracy. The accuracy analyses in sections 2 and 3 all follow the modified equation approach, applying truncated Taylor series expansions. The stability analyses in both sections simply apply the positive coefficients rule [29]. Next, on the basis of the same model equation, in section 4, the solvability properties (smoothing and convergence) of the favorite multi-D schemes from section 3 are investigated by Fourier analysis. Then in section 5, the favorite schemes as derived in section 3 for the model equation, are extended to the Euler equations. Further, in section 6, for the Euler equations, some techniques are considered for computing the specific flow-dependent rotation angle which is required at each cell face. Here, a novel technique is presented which makes use of the wave path in state space. Finally, in section 7, the theoretical results found in the previous sections are verified for some steady, fully supersonic Euler flows on the unit square; both flows with a contact discontinuity and flows with a shock wave.

5

2 Analysis of some grid-aligned 1-D upwind schemes

The analysis is performed for the linear, scalar, 2-D model equation

$$\cos\theta\frac{\partial u}{\partial x} + \sin\theta\frac{\partial u}{\partial y} = 0, \quad 0 \le \theta \le \frac{\pi}{2}, \tag{2.1a}$$

with θ the angle between the characteristic direction and the x-axis (Fig. 2.1). For ease of notation we introduce

$$\begin{pmatrix} a \\ b \end{pmatrix} \equiv \begin{pmatrix} \cos\theta \\ \sin\theta \end{pmatrix}. \tag{2.1b}$$

Considering the target equations, the steady 2-D Euler equations, it is clear that equation (2.1a) models these best for fully supersonic flow, with its real characteristic directions.
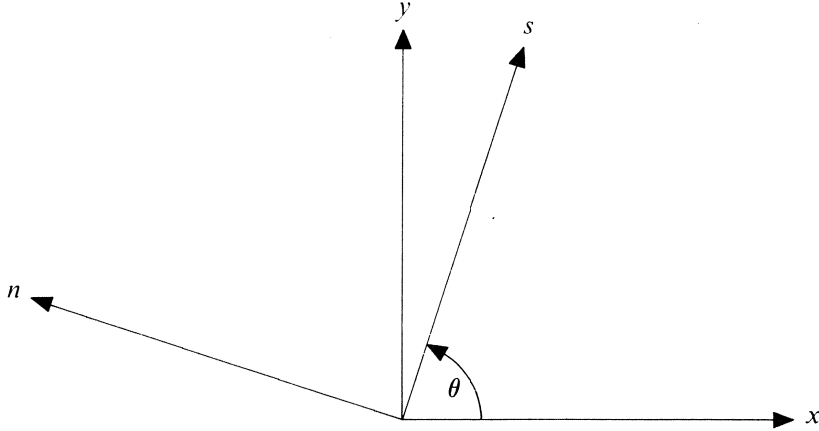

Fig. 2.1. Angle characteristic direction and characteristic coordinates.

2.1 First-order scheme on square grid

Discretization of the model equation on a square, cell-centered finite volume grid yields

$$a(u_{i+\frac{1}{2},j} - u_{i-\frac{1}{2},j}) + b(u_{i,j+\frac{1}{2}} - u_{i,j-\frac{1}{2}}) = 0, \tag{2.2}$$

where the half-integer indices refer to the cell faces between the (full-integer indexed) cell centers (Fig. 2.2). With the first-order, grid-aligned 1-D upwind scheme, given the positive sign of a and b, for the cell face states one takes

$$\begin{pmatrix} u_{i+\frac{1}{2},j} \\ u_{i,j+\frac{1}{2}} \end{pmatrix} = \begin{pmatrix} u_{i,j} \\ u_{i,j} \end{pmatrix}, \quad 0 \le \theta \le \frac{\pi}{2}. \tag{2.3}$$

Similar choices are made for $u_{i-\frac{1}{2},j}$ and $u_{i,j-\frac{1}{2}}$. Substituting these cell face states into (2.2) and applying truncated Taylor series expansions, one derives the modified equation

$$a\frac{\partial u}{\partial x} + b\frac{\partial u}{\partial y} - \frac{h}{2}\left[a\frac{\partial^2 u}{\partial x^2} + b\frac{\partial^2 u}{\partial y^2}\right] = O(h^2), \quad 0 \le \theta \le \frac{\pi}{2}. \tag{2.4}$$
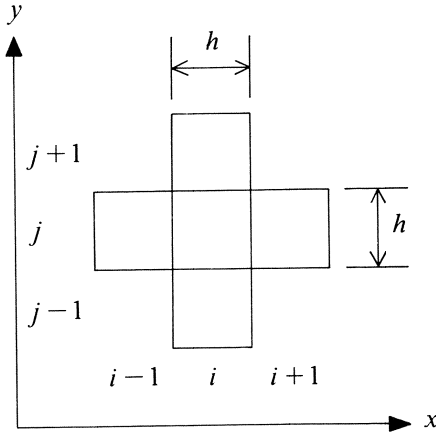
6

Fig. 2.2. Square finite volume i,j with neighbors.

By transformation to characteristic coordinates (Fig. 2.1), (2.4) becomes

$$\frac{\partial u}{\partial s} - \frac{h}{2}\left[(a^3 + b^3)\frac{\partial^2 u}{\partial s^2} - 2ab(a-b)\frac{\partial^2 u}{\partial s \partial n} + ab(a+b)\frac{\partial^2 u}{\partial n^2}\right] = O(h^2), \quad 0 \le \theta \le \frac{\pi}{2}. \quad (2.5)$$

For convenience we introduce the notations μ_{ss}, μ_{sn} and μ_{nn} for the coefficients of $\frac{\partial^2 u}{\partial s^2}, \frac{\partial^2 u}{\partial s \partial n}$ and $\frac{\partial^2 u}{\partial n^2}$, respectively. For the specific model equation considered here, the error term $\mu_{nn}\frac{\partial^2 u}{\partial n^2}$ in (2.5) is most detrimental to accuracy. (The other two error terms just vanish for the model equation; $\frac{\partial u}{\partial s} = 0$.) Hence, a higher-order accurate discretization can be constructed by only making μ_{nn} vanish. For the same model equation, compact multi-D upwind discretizations with only $\mu_{nn} = 0$, have been investigated already in [35]. However, no published results of that kind are available yet for the full Euler equations. In the present paper, we prefer compact multi-D upwind schemes with both $\mu_{sn} = 0$ and $\mu_{nn} = 0$; discretizations which guarantee a low diffusion for $\frac{\partial^2 u}{\partial s^2} = r(s, n)$, with $r(s, n)$ arbitrary, instead of $r(s, n) = 0$ only. In other words, we prefer discretizations which are more general by guaranteeing a certain order of accuracy for a specific model *operator* instead of for only a specific model *equation*. Further, we do make the extension from the linear scalar model operator to the Euler operator.

Definition 2.1
Consider the general modified equation

$$\frac{\partial u}{\partial s} - \frac{h}{2}\left[\mu_{ss}\frac{\partial^2 u}{\partial s^2} + \mu_{sn}\frac{\partial^2 u}{\partial s \partial n} + \mu_{nn}\frac{\partial^2 u}{\partial n^2}\right] = O(h^2), \quad 0 \le \theta \le \frac{\pi}{2}. \quad (2.6)$$

In this paper, $(\mu_{sn}, \mu_{nn})^T$ is called the *crosswind diffusion* and schemes for which $(\mu_{sn}, \mu_{nn})^T = 0$ are called *zero-crosswind diffusion schemes*.

From (2.5) it appears that for the first-order scheme (2.3), zero-crosswind diffusion occurs only in case of $\theta = 0$ or $\theta = \frac{\pi}{2}$, i.e. in case of grid-alignment of the characteristic directions. As opposed to these poor accuracy properties, the stability properties of first-order upwind scheme (2.3) are known to be good; the scheme does not allow unstable, oscillatory solutions. This results from the fact that the positive coefficients rule [29] is satisfied, which clearly appears from its stencil

$$\begin{bmatrix} \cdot & \cdot & \cdot \\ -a & a+b & \cdot \\ \cdot & -b & \cdot \end{bmatrix}, \quad 0 \le \theta \le \frac{\pi}{2}. \quad (2.7)$$

7

Definition 2.2

Consider the general discrete equation

$$\alpha_{i,j} u_{i,j} = \sum_{m=1}^{M} \sum_{n=1}^{N} \alpha_{i\pm m, j\pm n} u_{i\pm m, j\pm n}, \quad M \geq 1, N \geq 1. \tag{2.8}$$

In this paper, discrete equations satisfying the positive coefficients rule

$$\alpha_{i,j} \geq 0, \quad \alpha_{i\pm m, j\pm n} \geq 0, \quad \forall\, m, n, \tag{2.9}$$

are called *positive*.

2.2 First-order scheme on characteristic-aligned grid

From Euler practice, the positive effect of solution-adaptive grid-alignment is well-known. Here, for model equation (2.1a), we still demonstrate this effect for the alignment shown in Fig. 2.3. (As it were, the grid in Fig. 2.3 has been generated from the one in Fig. 2.2 by aligning all vertical cell faces with the characteristic direction.) The finite volume equation on this characteristic-aligned grid simply reads

$$u_{i,j+\frac{1}{2}} - u_{i,j-\frac{1}{2}} = 0. \tag{2.10}$$

There is no flux contribution from the characteristic-aligned cell faces; across each of these faces, the flux equals zero. Considering again first-order, grid-aligned 1-D upwinding, we now find as modified equation in characteristic coordinates

$$\frac{\partial u}{\partial s} - \frac{h}{2} \frac{\partial^2 u}{\partial s^2} = O(h^2), \tag{2.11}$$

which clearly shows the positive impact of grid-alignment on the reduction of crosswind diffusion. Further, despite the decreased diffusion, the discretization is still positive. Though promising at first sight, as already mentioned in section 1.2, for general Euler flows, solution-adaptive grid-alignment may lead to excessively complex grids and is therefore not attractive in general.
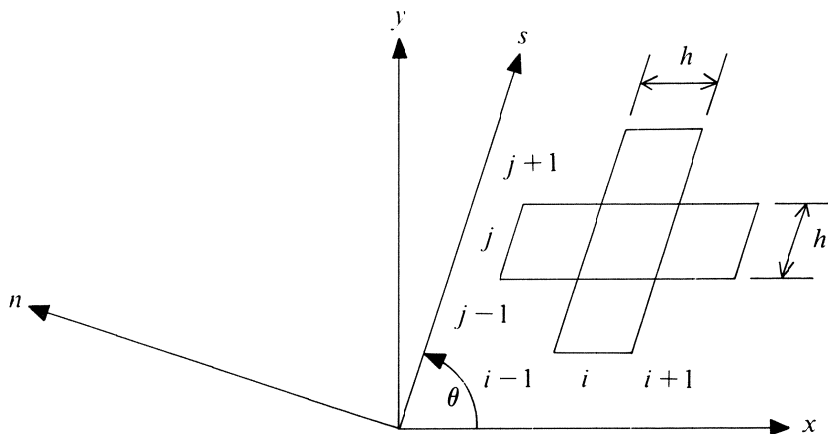

Fig. 2.3. Characteristic-aligned finite volume *i,j* with neighbors.

8

2.3 Higher-order schemes on square grid

Before considering multi-D upwind schemes, we also still investigate higher-order, grid-aligned 1-D upwind schemes. Higher-order 1-D upwind schemes are easily constructed by piecewise polynomial state interpolation through e.g. the κ-scheme [21]. Considering again the square finite volume grid (Fig. 2.2), with the κ-scheme one takes in equation (2.2):

$$
\begin{pmatrix} u_{i+\frac{1}{2},j} \\ u_{i,j+\frac{1}{2}} \end{pmatrix} = \begin{pmatrix} u_{i,j} + \frac{1+\kappa}{4}(u_{i+1,j} - u_{i,j}) + \frac{1-\kappa}{4}(u_{i,j} - u_{i-1,j}) \\ u_{i,j} + \frac{1+\kappa}{4}(u_{i,j+1} - u_{i,j}) + \frac{1-\kappa}{4}(u_{i,j} - u_{i,j-1}) \end{pmatrix}, \quad -1 \leq \kappa \leq 1, \quad 0 \leq \theta \leq \frac{\pi}{2}.
$$
(2.12)

Making similar choices for $u_{i-\frac{1}{2},j}$ and $u_{i,j-\frac{1}{2}}$, substituting these polynomial expressions into (2.2) and applying truncated Taylor series expansions, the following modified equation is found

$$
a\frac{\partial u}{\partial x} + b\frac{\partial u}{\partial y} + h^2\frac{\kappa - \frac{1}{3}}{4}\left[a\frac{\partial^3 u}{\partial x^3} + b\frac{\partial^3 u}{\partial y^3}\right] = \mathrm{O}(h^3), \quad 0 \leq \theta \leq \frac{\pi}{2},
$$
(2.13)

or, transformed to characteristic coordinates:

$$
\frac{\partial u}{\partial s} + h^2\frac{\kappa - \frac{1}{3}}{4}\left[(a^4 + b^4)\frac{\partial^3 u}{\partial s^3} - 3ab(a^2 - b^2)\frac{\partial^3 u}{\partial s^2 \partial n} + \right.
$$
$$
\left. 6a^2b^2\frac{\partial^3 u}{\partial s\partial n^2} + ab(a^2 - b^2)\frac{\partial^3 u}{\partial n^3}\right] = \mathrm{O}(h^3), \quad 0 \leq \theta \leq \frac{\pi}{2}.
$$
(2.14)

Comparing (2.14) with (2.5), it appears that the accuracy has been raised by a factor $\mathrm{O}(h)$. For $\kappa = \frac{1}{3}$, this is even a factor $\mathrm{O}(h^2)$. However, from the corresponding stencil

$$
\begin{bmatrix} \cdot & \cdot & \cdot & \cdot & \cdot \\ \cdot & \cdot & \frac{1+\kappa}{4}b & \cdot & \cdot \\ \frac{1-\kappa}{4}a & \frac{-5+3\kappa}{4}a & \frac{3(1-\kappa)}{4}(a+b) & \frac{1+\kappa}{4}a & \cdot \\ \cdot & \cdot & \frac{-5+3\kappa}{4}b & \cdot & \cdot \\ \cdot & \cdot & \frac{1-\kappa}{4}b & \cdot & \cdot \end{bmatrix}, \quad 0 \leq \theta \leq \frac{\pi}{2},
$$
(2.15)

it appears that the scheme's stability properties are less good; for any $\kappa \in [-1, 1]$, the discretization is non-positive.

3 Analysis of some multi-D upwind schemes

In the previous section, by the grid-aligned 1-D upwind schemes (2.3) and (2.12), the conflict between accuracy and stability (solvability) has been illustrated and a reference has been set for developing multi-D upwind schemes which yield a more proper balance between accuracy and solvability. For the scalar, linear convection operator and the square, cell-centered finite volume grid, we seek upwind schemes which preferably satisfy the following properties: (i) zero-crosswind diffusion, (ii) positivity, (iii) compactness, (iv) good smoothing of point Gauss-Seidel relaxation, and (v) continuous differentiability. The property of zero-crosswind diffusion is meant to lead to an accurate resolution of oblique layers. Positivity is strived for to avoid instabilities (without invoking a limiter). Compactness is to assure consistent boundary condition treatments. Good smoothing of point Gauss-Seidel relaxation should assure a fruitful application of multigrid, and continuous differentiability finally is required because of the intended application of Newton iteration inside the point relaxation.

3.1 Positive schemes

Multi-D upwind schemes which are most compact, i.e. 4-point compact, use

$$\begin{pmatrix} u_{i+\frac{1}{2},j} \\ u_{i,j+\frac{1}{2}} \end{pmatrix} = \begin{pmatrix} \delta(\theta)u_{i,j} + (1-\delta(\theta))\,u_{i,j-1} \\ \delta(\frac{\pi}{2}-\theta)u_{i,j} + (1-\delta(\frac{\pi}{2}-\theta))\,u_{i-1,j} \end{pmatrix}, \quad 0 \le \theta \le \frac{\pi}{2}. \tag{3.1a}$$

The coefficient $\delta(\theta)$ determines the scheme. To prevent unphysical features such as e.g. negative densities, we take it in the range $[0,1]$; $0 \le \delta(\theta) \le 1$. Notice that symmetry of scheme (3.1a) with respect to $\theta = \frac{\pi}{4}$ is guaranteed. For ease of notation, we introduce

$$\begin{pmatrix} \delta_1(\theta) \\ \delta_2(\theta) \end{pmatrix} \equiv \begin{pmatrix} \delta(\theta) \\ \delta(\frac{\pi}{2}-\theta) \end{pmatrix}. \tag{3.1b}$$

Then, the 4-point stencil corresponding with (3.1a)-(3.1b) reads

$$\begin{bmatrix} \cdot & \cdot & \cdot \\ -\delta_1(\theta)a + (1-\delta_2(\theta))b & \delta_1(\theta)a + \delta_2(\theta)b & \cdot \\ -(1-\delta_1(\theta))a - (1-\delta_2(\theta))b & (1-\delta_1(\theta))a - \delta_2(\theta)b & \cdot \end{bmatrix}, \quad 0 \le \theta \le \frac{\pi}{2}. \tag{3.2}$$

In characteristic coordinates, the modified equation for scheme (3.1a)-(3.1b) reads

$$\frac{\partial u}{\partial s} - \frac{h}{2}\Bigg[((1+ab)(a+b) - 2(\delta_1 a + \delta_2 b)ab)\,\frac{\partial^2 u}{\partial s^2} +$$

$$2(a-b)(1+ab - (\delta_1 a + \delta_2 b)(a+b))\,\frac{\partial^2 u}{\partial s \partial n} +$$

$$2ab\left((\delta_1 - \frac{1}{2})a + (\delta_2 - \frac{1}{2})b\right)\frac{\partial^2 u}{\partial n^2}\Bigg] = O(h^2), \quad 0 \le \theta \le \frac{\pi}{2}. \tag{3.3}$$

The 4-point-compactness of scheme (3.1a)-(3.1b) results in a close relationship with first-order, grid-aligned 1-D upwind scheme (2.3). (In fact, 1-D upwind scheme (2.3) is also implied by (3.1a)-(3.1b); it is obtained by simply taking $\delta_1(\theta) = \delta_2(\theta) = 1$, $0 \le \theta \le \frac{\pi}{2}$.) For later comparisons, in Fig. 3.1a we show the values of the diffusion coefficients μ_{ss}, μ_{sn} and μ_{nn} for scheme (2.3). Further, in Fig. 3.1b we still show the values of the coefficients in stencil (2.7). By a solid line we indicate the diagonal coefficient, and by dashed lines the off-diagonal coefficients.
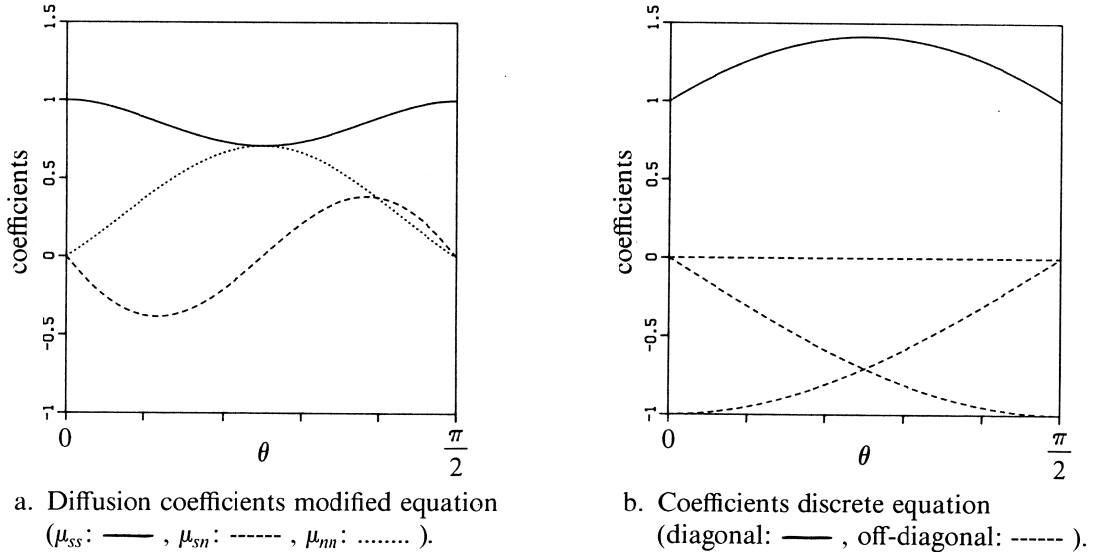

a. Diffusion coefficients modified equation
(μ_{ss}: —— , μ_{sn}: ------ , μ_{nn}: ....).

b. Coefficients discrete equation
(diagonal: —— , off-diagonal: ------).

Fig. 3.1. Coefficients first-order, grid-aligned 1-D upwind scheme (2.3).

3.1.1 A non-continuously differentiable scheme

As mentioned, the choice of $\delta_1(\theta)$ and $\delta_2(\theta)$ determines the scheme. The simplest solution-dependent multi-D choice is $\delta_1(\theta) = 1$, $\delta_2(\theta) = 0$ for $0 \leq \theta \leq \frac{\pi}{4}$ and hence $\delta_1(\theta) = 0$, $\delta_2(\theta) = 1$ for $\frac{\pi}{4} \leq \theta \leq \frac{\pi}{2}$. This leads to the cell face states

$$\begin{pmatrix} u_{i+\frac{1}{2},j} \\ u_{i,j+\frac{1}{2}} \end{pmatrix} = \begin{pmatrix} u_{i,j} \\ u_{i-1,j} \end{pmatrix}, \quad 0 \leq \theta \leq \frac{\pi}{4}, \tag{3.4a}$$

$$\begin{pmatrix} u_{i+\frac{1}{2},j} \\ u_{i,j+\frac{1}{2}} \end{pmatrix} = \begin{pmatrix} u_{i,j-1} \\ u_{i,j} \end{pmatrix}, \quad \frac{\pi}{4} \leq \theta \leq \frac{\pi}{2}, \tag{3.4b}$$

the stencils

$$\begin{bmatrix} \cdot & \cdot & \cdot \\ -a+b & a & \cdot \\ -b & \cdot & \cdot \end{bmatrix}, \quad 0 \leq \theta \leq \frac{\pi}{4}, \tag{3.5a}$$

$$\begin{bmatrix} \cdot & \cdot & \cdot \\ \cdot & b & \cdot \\ -a & a-b & \cdot \end{bmatrix}, \quad \frac{\pi}{4} \leq \theta \leq \frac{\pi}{2}, \tag{3.5b}$$

and the modified equations

$$\frac{\partial u}{\partial s} - \frac{h}{2} \left[\left(a + b^2(a+b)\right) \frac{\partial^2 u}{\partial s^2} + 2b^2(a-b) \frac{\partial^2 u}{\partial s \partial n} + ab(a-b) \frac{\partial^2 u}{\partial n^2} \right] = O(h^2), \quad 0 \leq \theta \leq \frac{\pi}{4}, \tag{3.6a}$$

$$\frac{\partial u}{\partial s} - \frac{h}{2} \left[\left(b + a^2(a+b)\right) \frac{\partial^2 u}{\partial s^2} + 2a^2(a-b) \frac{\partial^2 u}{\partial s \partial n} + ab(b-a) \frac{\partial^2 u}{\partial n^2} \right] = O(h^2), \quad \frac{\pi}{4} \leq \theta \leq \frac{\pi}{2}. \tag{3.6b}$$

As shown in Fig. 3.2a, this simple 4-point-compact upwind scheme already leads to a significant decrease in crosswind diffusion, when compared to the first-order, grid-aligned 1-D upwind scheme (Fig. 3.1a). Moreover, the scheme is still positive (Fig. 3.2b). Unfortunately, it is not continuously differentiable over the complete range of θ considered, and therefore it is not satisfactory for our purposes.

a. Diffusion coefficients modified equation
(μ_{ss}: ——— , μ_{sn}: ------ , μ_{nn}: ········).

b. Coefficients discrete equation
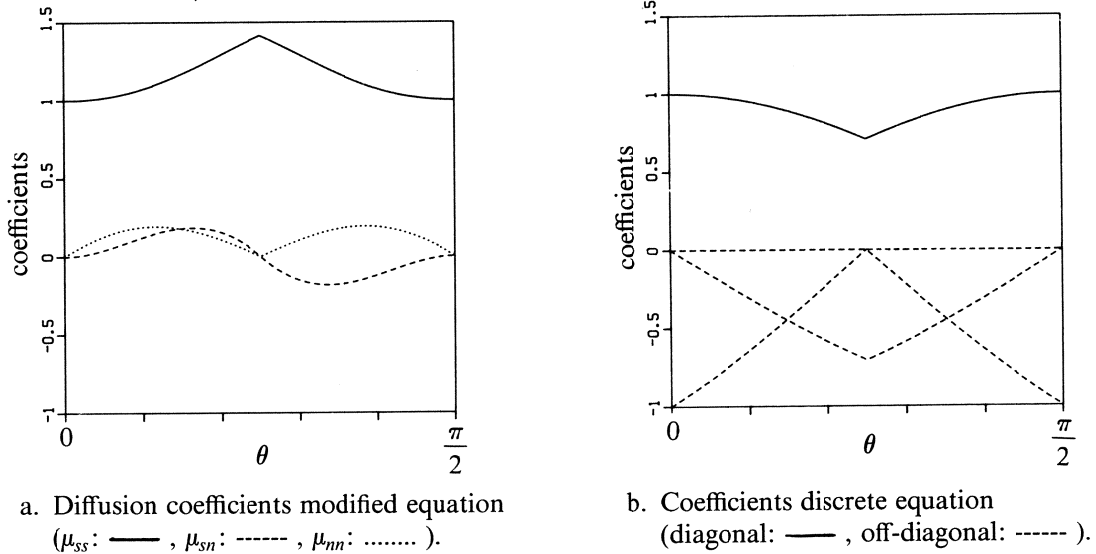(diagonal: ——— , off-diagonal: ------).

Fig. 3.2. Coefficients non-continuously differentiable scheme (3.4a)-(3.4b).

3.1.2 A continuously differentiable scheme

In an attempt to derive a positive, 4-point-compact upwind scheme which is continuously differentiable, we first try to make μ_{sn} and μ_{nn} equal to zero. From (3.3), $\mu_{sn} = 0$ and $\mu_{nn} = 0$ lead to respectively

$$\delta_1 a + \delta_2 b = \frac{1 + ab}{a + b}, \quad 0 \leq \theta \leq \frac{\pi}{2}, \tag{3.7a}$$

$$\delta_1 a + \delta_2 b = \frac{a + b}{2}, \quad 0 \leq \theta \leq \frac{\pi}{2}, \tag{3.7b}$$

which clearly is an inconsistent system of equations. This leads to the following theorem:

Theorem 3.1
No 4-point-compact upwind scheme exists for which both $\mu_{sn} = 0$ and $\mu_{nn} = 0$.

Next, we require only μ_{nn} to be zero, i.e. we require (3.7b) to hold. Further, following definition (2.1) and stencil (3.2), positivity requires

$$(\delta_1 a + \delta_2 b) \begin{pmatrix} 1 \\ 1 \\ 1 \\ -1 \end{pmatrix} \geq \begin{pmatrix} 0 \\ b \\ a \\ -a - b \end{pmatrix}, \quad 0 \leq \theta \leq \frac{\pi}{2}. \tag{3.8}$$

It appears that system (3.7b)-(3.8) is inconsistent as well. This leads to the theorem:

Theorem 3.2
No 4-point-compact upwind scheme exists which is positive and for which $\mu_{nn} = 0$.

Finally, we require $\mu_{sn} = 0$ to hold (i.e. (3.7a)) in combination with (3.8). It can be verified that this system has a solution. Assuming the form $\delta_1(\theta) = \frac{a + \alpha b}{a + b}$, α some constant, with symmetry relation (3.1b) we get $\delta_2(\theta) = \frac{b + \alpha a}{a + b}$. Substitution of these forms of $\delta_1(\theta)$ and $\delta_2(\theta)$ into (3.7a) yields $\alpha = \frac{1}{2}$, and hence

$$\begin{pmatrix} u_{i+\frac{1}{2},j} \\ u_{i,j+\frac{1}{2}} \end{pmatrix} = \begin{pmatrix} \frac{a + \frac{1}{2}b}{a+b} u_{i,j} + \frac{\frac{1}{2}b}{a+b} u_{i,j-1} \\ \frac{b + \frac{1}{2}a}{a+b} u_{i,j} + \frac{\frac{1}{2}a}{a+b} u_{i-1,j} \end{pmatrix}, \quad 0 \leq \theta \leq \frac{\pi}{2}, \tag{3.9}$$

which gives the stencil

$$\begin{bmatrix} \cdot & \cdot & \cdot \\ \frac{-a^2}{a+b} & \frac{1+ab}{a+b} & \cdot \\ \frac{-ab}{a+b} & \frac{-b^2}{a+b} & \cdot \end{bmatrix}, \quad 0 \leq \theta \leq \frac{\pi}{2}, \tag{3.10}$$

and the modified equation

$$\frac{\partial u}{\partial s} - \frac{h}{2} \left[\frac{1 + ab}{a + b} \frac{\partial^2 u}{\partial s^2} + \frac{ab}{a + b} \frac{\partial^2 u}{\partial n^2} \right] = O(h^2), \quad 0 \leq \theta \leq \frac{\pi}{2}. \tag{3.11}$$

Analogous to Figs. 3.1 and 3.2, in Fig. 3.3 we show the coefficients of scheme (3.9). The non-continuous differentiability *but* zero-crosswind diffusion at $\theta = \frac{\pi}{4}$ of scheme (3.4a)-(3.4b) has been replaced in the present scheme by a continuous differentiability *but* non-zero-crosswind diffusion at $\theta = \frac{\pi}{4}$. The scheme's crosswind diffusion is significantly lower than that of the first-order, grid-aligned 1-D upwind scheme (Fig. 3.1a). This in combination with the properties of positivity and continuous differentiability makes that multi-D upwind scheme (3.9) is a more appropriate candidate for our multigrid purposes than first-order, grid-aligned 1-D upwind scheme (2.3). We notice that in another way and in another context, scheme (3.9) is also derived in [20].
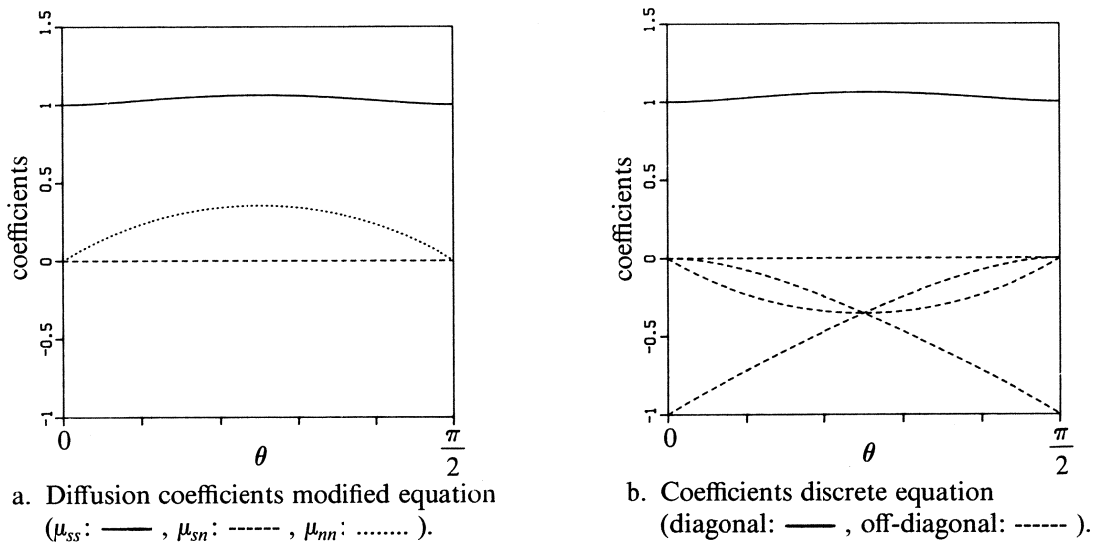
12

a. Diffusion coefficients modified equation
(μ_{ss}: ——— , μ_{sn}: ------ , μ_{nn}: ········).

b. Coefficients discrete equation
(diagonal: ——— , off-diagonal: ------).

Fig. 3.3. Coefficients continuously differentiable scheme (3.9).

3.2 Non-positive schemes

3.2.1 A very simple scheme

Before considering wider stencils, in this subsection we still restrict ourselves to the 4-point-compact stencil (3.2). Theorem 3.2 does not exclude the existence of a non-positive, 4-point-compact upwind scheme for which $\mu_{nn} = 0$. Diffusion condition (3.7b) is satisfied by e.g. $\delta_1(\theta) = \frac{1}{2}$, $\delta_2(\theta) = \frac{1}{2}$, $0 \le \theta \le \frac{\pi}{2}$, leading to the cell face states

$$\begin{pmatrix} u_{i+\frac{1}{2},j} \\ u_{i,j+\frac{1}{2}} \end{pmatrix} = \begin{pmatrix} \frac{1}{2}u_{i,j} + \frac{1}{2}u_{i,j-1} \\ \frac{1}{2}u_{i,j} + \frac{1}{2}u_{i-1,j} \end{pmatrix}, \quad 0 \le \theta \le \frac{\pi}{2}, \tag{3.12}$$

the stencil

$$\begin{bmatrix} \cdot & \cdot & \cdot \\ -\frac{1}{2}(a-b) & \frac{1}{2}(a+b) & \cdot \\ -\frac{1}{2}(a+b) & \frac{1}{2}(a-b) & \cdot \end{bmatrix}, \quad 0 \le \theta \le \frac{\pi}{2}, \tag{3.13}$$

and the modified equation

$$\frac{\partial u}{\partial s} - \frac{h}{2}\left[(a+b)\frac{\partial^2 u}{\partial s^2} + (a-b)\frac{\partial^2 u}{\partial s \partial n}\right] = O(h^2), \quad 0 \le \theta \le \frac{\pi}{2}. \tag{3.14}$$

Notice that though scheme (3.12) is multi-D upwind, as opposed to the foregoing multi-D upwind schemes (3.4a)-(3.4b) and (3.9), it is solution-independent in the range $0 < \theta < \frac{\pi}{2}$. Also notice that scheme (3.12) is an example of a 4-point-compact scheme which is higher than first-order accurate for the model equation considered. (Substituting the model equation, $\frac{\partial u}{\partial s} = 0$, into the first-order error term, it vanishes completely.) As mentioned in section 2.1, in this paper we prefer discretizations which guarantee a certain order of accuracy for a differential *operator*. To conclude, in Fig. 3.4 we give a detailed account of the present scheme's diffusion and positivity properties. Notice that the behavior of μ_{sn} is not really good.

13

a. Diffusion coefficients modified equation
(μ_{ss}: ——— , μ_{sn}: ------ , μ_{nn}: ....).

b. Coefficients discrete equation
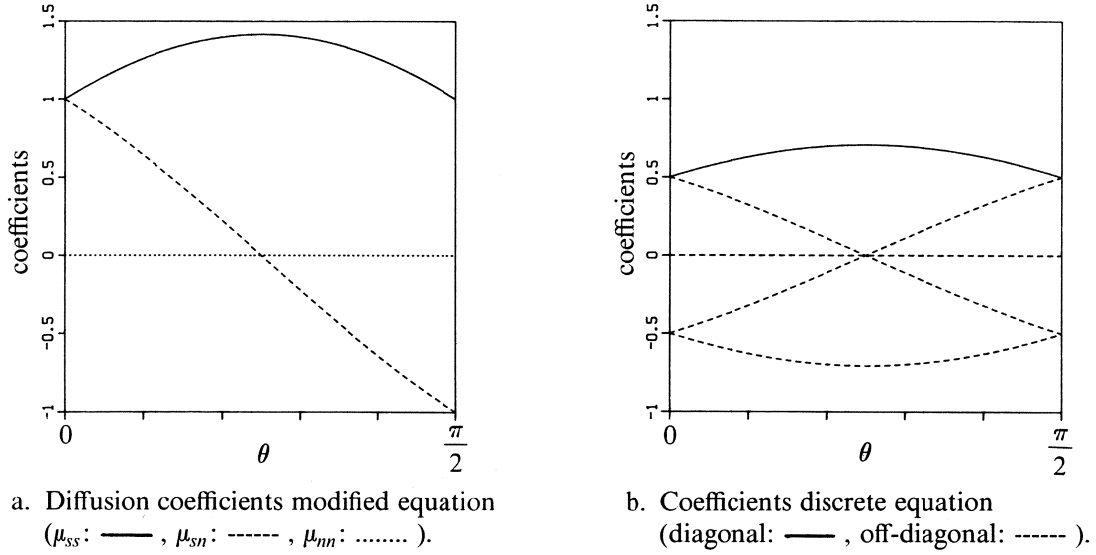(diagonal: ——— , off-diagonal: ------).

Fig. 3.4. Coefficients non-positive scheme (3.12).

3.2.2 A characteristic-aligned scheme

The natural way for removing all crosswind diffusion in determining the cell face states $u_{i+\frac{1}{2},j}$ and $u_{i,j+\frac{1}{2}}$ seems to be extrapolation in the exact characteristic direction. Striving for the greatest compactness, the extrapolation should be done from the nearest line connecting two cell center states. Avoiding negative coefficients to prevent unphysical features such as e.g. negative densities, for the situation illustrated in Fig. 3.5 we apply

$$\begin{pmatrix} u_{i+\frac{1}{2},j} \\ u_{i,j+\frac{1}{2}} \end{pmatrix} = \begin{pmatrix} (1 - \frac{1}{2}\frac{b}{a})u_{i,j} + \frac{1}{2}\frac{b}{a}u_{i,j-1} \\ (\frac{1}{2} + \frac{b}{a})u_{i-1,j} + (\frac{1}{2} - \frac{b}{a})u_{i-1,j+1} \end{pmatrix}, \quad 0 \le \theta \le \arctan\frac{1}{2}. \tag{3.15a}$$
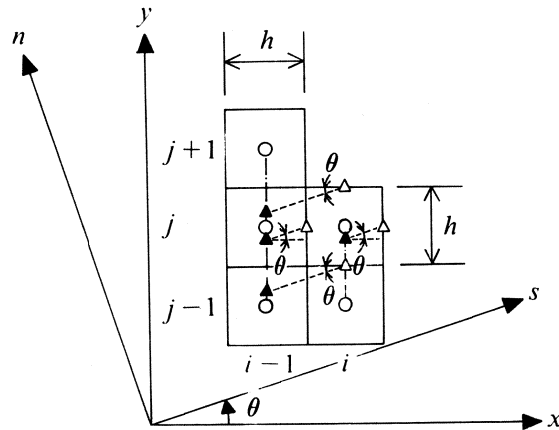

Fig. 3.5. Geometric interpretation characteristic-aligned scheme, $0 \le \theta \le \arctan\frac{1}{2}$
(◯: cell center state, △: cell face state, ▲: extrapolant).

14

For the other subranges of θ, following the same strategy, we apply

$$\begin{pmatrix} u_{i+\frac{1}{2},j} \\ u_{i,j+\frac{1}{2}} \end{pmatrix} = \begin{pmatrix} (1 - \frac{1}{2}\frac{b}{a})u_{i,j} + \frac{1}{2}\frac{b}{a}u_{i,j-1} \\ (1 - \frac{1}{2}\frac{a}{b})u_{i,j} + \frac{1}{2}\frac{a}{b}u_{i-1,j} \end{pmatrix}, \quad \arctan\frac{1}{2} \leq \theta \leq \arctan 2, \qquad (3.15b)$$

$$\begin{pmatrix} u_{i+\frac{1}{2},j} \\ u_{i,j+\frac{1}{2}} \end{pmatrix} = \begin{pmatrix} (\frac{1}{2} + \frac{a}{b})u_{i,j-1} + (\frac{1}{2} - \frac{a}{b})u_{i+1,j-1} \\ (1 - \frac{1}{2}\frac{a}{b})u_{i,j} + \frac{1}{2}\frac{a}{b}u_{i-1,j} \end{pmatrix}, \quad \arctan 2 \leq \theta \leq \frac{\pi}{2}. \qquad (3.15c)$$

We notice that for the subrange $\arctan\frac{1}{2} \leq \theta \leq \arctan 2$, the present scheme - so (3.15b) - is identical to the so-called 2-D scheme from [35].

The stencils corresponding with (3.15a)-(3.15c) are

$$\begin{bmatrix} b(\frac{1}{2} - \frac{b}{a}) & \cdot & \cdot \\ -a + b(\frac{1}{2} + 2\frac{b}{a}) & a - \frac{1}{2}b & \cdot \\ -b(1 + \frac{b}{a}) & \frac{1}{2}b & \cdot \end{bmatrix}, \quad 0 \leq \theta \leq \arctan\frac{1}{2}, \qquad (3.16a)$$

$$\begin{bmatrix} \cdot & \cdot & \cdot \\ -\frac{1}{2}(a - b) & \frac{1}{2}(a + b) & \cdot \\ -\frac{1}{2}(a + b) & \frac{1}{2}(a - b) & \cdot \end{bmatrix}, \quad \arctan\frac{1}{2} \leq \theta \leq \arctan 2, \qquad (3.16b)$$

$$\begin{bmatrix} \cdot & \cdot & \cdot \\ \frac{1}{2}a & b - \frac{1}{2}a & \cdot \\ -a(1 + \frac{a}{b}) & -b + a(\frac{1}{2} + 2\frac{a}{b}) & a(\frac{1}{2} - \frac{a}{b}) \end{bmatrix}, \quad \arctan 2 \leq \theta \leq \frac{\pi}{2}. \qquad (3.16c)$$

Notice that, though wider than the 4-point-compact stencils, the present stencils are still more compact than e.g. (2.15). A consistent boundary condition treatment is still possible. Also notice that for $\arctan\frac{1}{2} \leq \theta \leq \arctan 2$, stencil (3.16b) is identical to stencil (3.13), although the corresponding schemes are different.

The modified equations corresponding with (3.15a)-(3.15c) read

$$\frac{\partial u}{\partial s} - \frac{h}{2}\left[\frac{1 + b^2}{a}\frac{\partial^2 u}{\partial s^2} + b\frac{\partial^2 u}{\partial s \partial n}\right] = O(h^2), \quad 0 \leq \theta \leq \arctan\frac{1}{2}, \qquad (3.17a)$$

$$\frac{\partial u}{\partial s} - \frac{h}{2}\left[(a + b)\frac{\partial^2 u}{\partial s^2} + (a - b)\frac{\partial^2 u}{\partial s \partial n}\right] = O(h^2), \quad \arctan\frac{1}{2} \leq \theta \leq \arctan 2, \qquad (3.17b)$$

$$\frac{\partial u}{\partial s} - \frac{h}{2}\left[\frac{1 + a^2}{b}\frac{\partial^2 u}{\partial s^2} - a\frac{\partial^2 u}{\partial s \partial n}\right] = O(h^2), \quad \arctan 2 \leq \theta \leq \frac{\pi}{2}. \qquad (3.17c)$$

As for scheme (3.12), we have $\mu_{nn} = 0$ over the complete range of θ considered. Yet, disregarding our specific model equation ($\frac{\partial u}{\partial s} = 0$), the crosswind diffusion is still non-zero, leading to the following remark.

Remark 3.1
Characteristic-aligned extrapolation does not necessarily result in zero-crosswind diffusion.

In Fig. 3.6 we give the present scheme's coefficients graphs. Notice that the conditional branching introduced with scheme (3.15a)-(3.15c) leads to better diffusion properties than those of 4-point-compact scheme (3.12) (Fig. 3.4a); whereas the corresponding diffusion properties are identical in the subrange $\arctan\frac{1}{2} \leq \theta \leq \arctan 2$, in the subranges $0 \leq \theta \leq \arctan\frac{1}{2}$ and $\arctan 2 \leq \theta \leq \frac{\pi}{2}$, scheme (3.15a)-(3.15c) is clearly less diffusive.
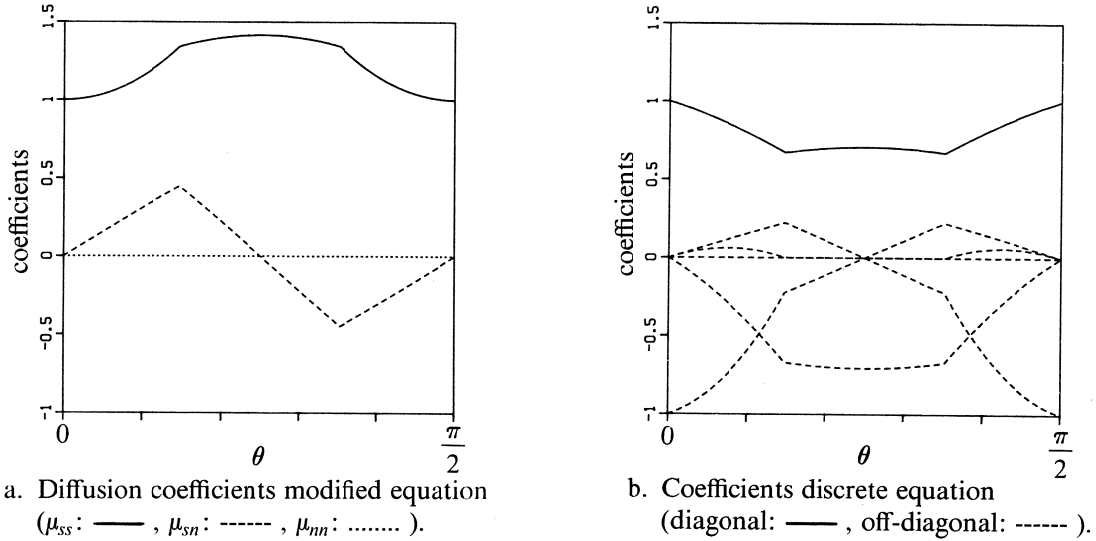
a. Diffusion coefficients modified equation
(μ_{ss}: ——— , μ_{sn}: ------ , μ_{nn}: ....).

b. Coefficients discrete equation
(diagonal: ——— , off-diagonal: ------).

Fig. 3.6. Coefficients characteristic-aligned scheme (3.15a)-(3.15c).

3.2.3 A zero-crosswind diffusion scheme

Deriving a scheme with zero-crosswind diffusion (over the complete range of θ considered), we follow again the modified equation approach. To start, we consider the situation as illustrated in Fig. 3.5, a situation with small θ. Striving for compactness, the extrapolation is done again from the nearest lines connecting two neighboring cell center states, also avoiding negative coefficients:

$$\begin{pmatrix} u_{i+\frac{1}{2},j} \\ u_{i,j+\frac{1}{2}} \end{pmatrix} = \begin{pmatrix} \delta_1(\theta)u_{i,j} + (1 - \delta_1(\theta))\,u_{i,j-1} \\ \delta_2(\theta)u_{i-1,j} + (1 - \delta_2(\theta))\,u_{i-1,j+1} \end{pmatrix}, \quad 0 \leq \delta_1(\theta), \delta_2(\theta) \leq 1, \quad 0 \leq \theta \leq \theta_{up},$$

(3.18)

with the (small) upper bound θ_{up} still unspecified. We remark that just as with the foregoing 4-point-compact schemes, here $\delta_1(\theta)$ and $\delta_2(\theta)$ also are symmetric with respect to $\theta = \frac{\pi}{4}$; cf. (3.1b). With (3.18), we derive the following modified equation

$$\frac{\partial u}{\partial s} - \frac{h}{2} \left[\left(a^3 + 2(1 - \delta_1)a^2b + 2ab^2 + (2\delta_2 - 1)b^3\right) \frac{\partial^2 u}{\partial s^2} + \right.$$

$$2\left((1 - \delta_1)a^3 + (\delta_1 + 2\delta_2 - 2)ab^2 - b^3\right) \frac{\partial^2 u}{\partial s \partial n} +$$

$$\left. ab\left((2\delta_1 + 2\delta_2 - 3)a - b\right) \frac{\partial^2 u}{\partial n^2} \right] = O(h^2), \quad 0 \leq \theta \leq \theta_{up}.$$

(3.19)

From (3.19), it follows that no crosswind diffusion occurs for $\delta_1(\theta) = 1$, $\delta_2(\theta) = \frac{1}{2}(1 + \frac{b}{a})$, $0 \leq \theta \leq \theta_{up} = \frac{\pi}{4}$, where the indicated θ-range (with $\theta_{up} = \frac{\pi}{4}$) is that for which negative coefficients (so unphysical features) are just avoided. A geometric interpretation is given in Fig. 3.7a. For the remaining subrange $\frac{\pi}{4} \leq \theta \leq \frac{\pi}{2}$, we deal with the symmetric counterpart of (3.18);

$$\begin{pmatrix} u_{i+\frac{1}{2},j} \\ u_{i,j+\frac{1}{2}} \end{pmatrix} = \begin{pmatrix} \delta_1(\theta)u_{i,j-1} + (1 - \delta_1(\theta))\,u_{i+1,j-1} \\ \delta_2(\theta)u_{i,j} + (1 - \delta_2(\theta))\,u_{i-1,j} \end{pmatrix}, \quad 0 \leq \delta_1(\theta), \delta_2(\theta) \leq 1, \quad \frac{\pi}{4} \leq \theta \leq \frac{\pi}{2},$$

(3.20)

for which we can write down immediately: $\delta_1(\theta) = \frac{1}{2}(1 + \frac{a}{b})$, $\delta_2(\theta) = 1$, $\frac{\pi}{4} \leq \theta \leq \frac{\pi}{2}$. A geometric interpretation is given in Fig. 3.7b.
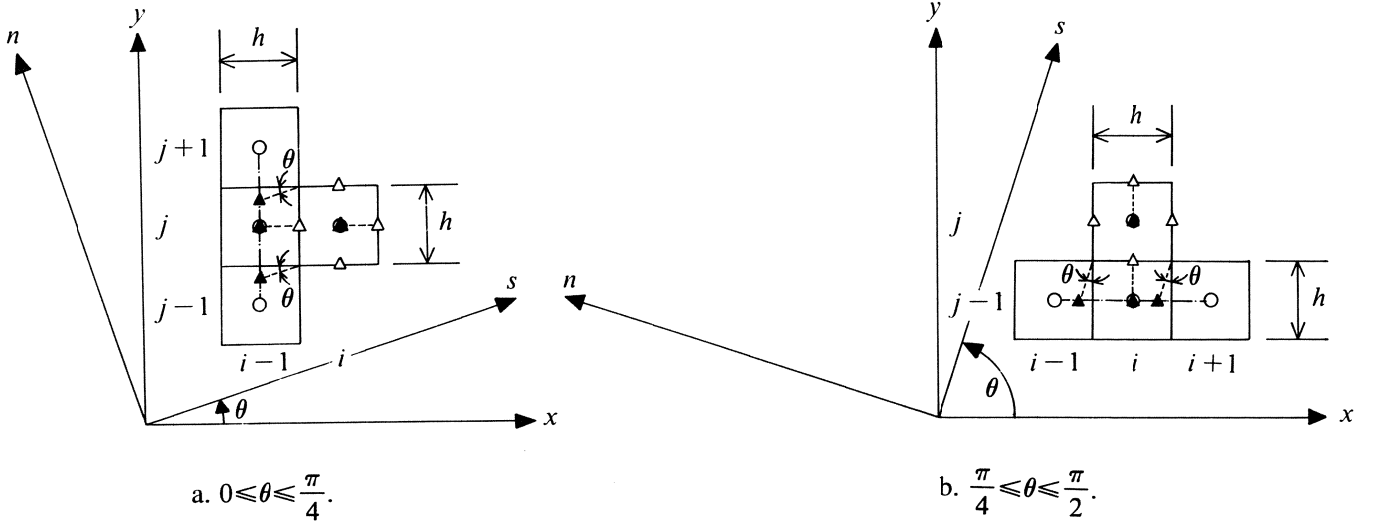
16

Fig. 3.7. Geometric interpretation zero-crosswind diffusion scheme (3.21a)-(3.21b)
($\bigcirc$: cell center state, $\triangle$: cell face state, $\blacktriangle$: extrapolant).

Summarizing, we have derived as expressions for the cell face states:

$$\begin{pmatrix} u_{i+\frac{1}{2},j} \\ u_{i,j+\frac{1}{2}} \end{pmatrix} = \begin{pmatrix} u_{i,j} \\ \frac{1}{2}(1+\frac{b}{a})u_{i-1,j} + \frac{1}{2}(1-\frac{b}{a})u_{i-1,j+1} \end{pmatrix}, \quad 0 \le \theta \le \frac{\pi}{4}, \tag{3.21a}$$

$$\begin{pmatrix} u_{i+\frac{1}{2},j} \\ u_{i,j+\frac{1}{2}} \end{pmatrix} = \begin{pmatrix} \frac{1}{2}(1+\frac{a}{b})u_{i,j-1} + \frac{1}{2}(1-\frac{a}{b})u_{i+1,j-1} \\ u_{i,j} \end{pmatrix}, \quad \frac{\pi}{4} \le \theta \le \frac{\pi}{2}, \tag{3.21b}$$

as corresponding stencils:

$$\begin{bmatrix} \frac{1}{2}b(1-\frac{b}{a}) & \cdot & \cdot \\ b(\frac{b}{a}-\frac{a}{b}) & a & \cdot \\ -\frac{1}{2}b(1+\frac{b}{a}) & \cdot & \cdot \end{bmatrix}, \quad 0 \le \theta \le \frac{\pi}{4}, \tag{3.22a}$$

$$\begin{bmatrix} \cdot & \cdot & \cdot \\ \cdot & b & \cdot \\ -\frac{1}{2}a(1+\frac{a}{b}) & a(\frac{a}{b}-\frac{b}{a}) & \frac{1}{2}a(1-\frac{a}{b}) \end{bmatrix}, \quad \frac{\pi}{4} \le \theta \le \frac{\pi}{2}, \tag{3.22b}$$

and as modified equations:

$$\frac{\partial u}{\partial s} - \frac{h}{2}\frac{1}{a}\frac{\partial^2 u}{\partial s^2} = O(h^2), \quad 0 \le \theta \le \frac{\pi}{4}, \tag{3.23a}$$

$$\frac{\partial u}{\partial s} - \frac{h}{2}\frac{1}{b}\frac{\partial^2 u}{\partial s^2} = O(h^2), \quad \frac{\pi}{4} \le \theta \le \frac{\pi}{2}. \tag{3.23b}$$

A remarkable property of zero-crosswind diffusion scheme (3.21a)-(3.21b) when compared to characteristic-aligned scheme (3.15a)-(3.15c) is its greater simplicity, despite its better accuracy. In Fig. 3.8 we give its diffusion and positivity properties.
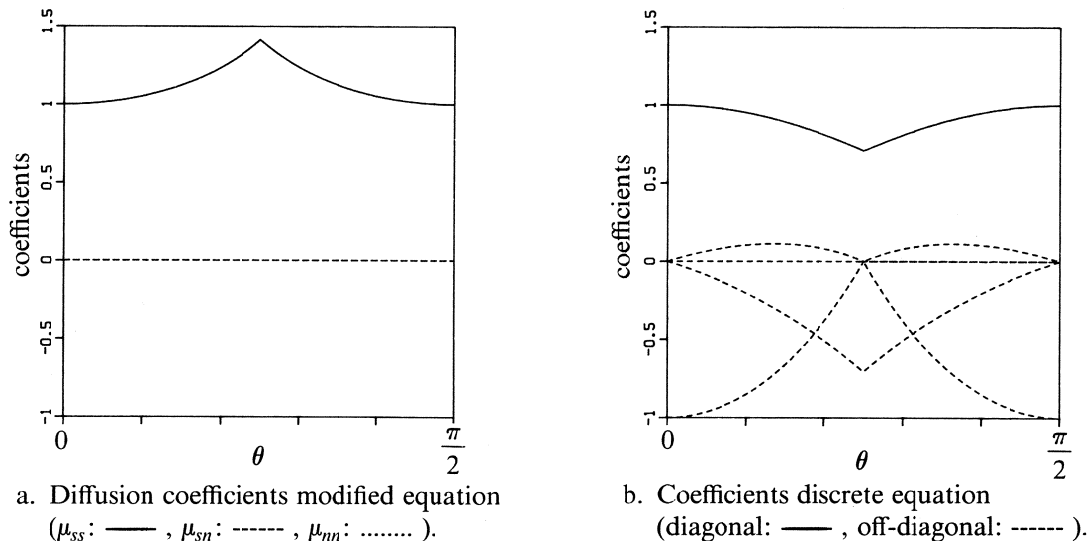
a. Diffusion coefficients modified equation
(μ_{ss}: ——— , μ_{sn}: ------ , μ_{nn}: ....).

b. Coefficients discrete equation
(diagonal: ——— , off-diagonal: ------).

Fig. 3.8. Coefficients zero-crosswind diffusion scheme (3.21a)-(3.21b).

4 Analysis of multigrid and defect correction iteration

In the foregoing section, two promising multi-D upwind schemes have been derived; one is positive, the other is non-positive. The positive scheme - scheme (3.9) - is 4-point-compact, continuously differentiable, low-diffusive in crosswind direction, but possibly still enough diffusive to allow a good smoothing of point Gauss-Seidel relaxation and hence a successful application of multigrid iteration. The non-positive scheme - scheme (3.21a)-(3.21b) - is 6-point-compact, zero-crosswind-diffusive and hence most promising from the viewpoint of accuracy. Due to its non-positivity, it is already known that the discretized equations corresponding with the zero-crosswind diffusion scheme cannot be efficiently solved by means of multigrid iteration.

In the present section, we analyze some solution methods for the schemes (3.9) and (3.21a)-(3.21b). The analysis is made again for model equation (2.1a)-(2.1b) on a square, cell-centered finite volume grid. In view of the multigrid solution, for scheme (3.9) the smoothing behavior of point Gauss-Seidel relaxation is investigated. This smoothing behavior is compared with that of 1-D upwind scheme (2.3). To solve the system of equations for zero-crosswind diffusion scheme (3.21a)-(3.21b), we rely on defect correction iteration [7, 16, 17], with (possibly) continuously differentiable scheme (3.9) as the 'working horse' in the inner multigrid iteration. In [35], it is stated that defect correction iteration is not a fully efficient solution technique for non-elliptic problems, and there direct multigrid is preferred. To our opinion, direct multigrid does not allow sufficiently accurate solutions, because the smoothing procedure requires too dissipative discretizations. When considering the convergence in some general error norm, we agree that for non-elliptic problems, defect correction iteration is not fully efficient. (See e.g. [4] and [8] for theoretical and experimental evidence on this.) However, considering - instead of the error's convergence to zero - the solution's convergence to higher-order accuracy, one gets a more satisfactory picture, both in theory [6] and in practice [7, 16, 17].

4.1 Smoothing of point Gauss-Seidel relaxation

To study the smoothing of lexicographical point Gauss-Seidel relaxation, eight different relaxation sweep directions can be considered: (i) downwind, upwind, crosswind up and crosswind down, each with the i-loop as the inner loop, and (ii) downwind, upwind and crosswind up and down, each with the j-loop as the inner loop. All eight directions are considered for the complete range of θ; $\theta \in [0, \frac{\pi}{2}]$. Introducing n for the number of sweeps performed, the eight possibilities are illustrated in Fig. 4.1.

Downwind:
$$\begin{bmatrix} u^n & u^n & u^n \\ u^{n+1} & u^{n+1} & u^n \\ u^{n+1} & u^{n+1} & u^{n+1} \end{bmatrix} \qquad \begin{bmatrix} u^{n+1} & u^n & u^n \\ u^{n+1} & u^{n+1} & u^n \\ u^{n+1} & u^{n+1} & u^n \end{bmatrix}$$

Upwind:
$$\begin{bmatrix} u^{n+1} & u^{n+1} & u^{n+1} \\ u^n & u^{n+1} & u^{n+1} \\ u^n & u^n & u^n \end{bmatrix} \qquad \begin{bmatrix} u^n & u^{n+1} & u^{n+1} \\ u^n & u^{n+1} & u^{n+1} \\ u^n & u^n & u^{n+1} \end{bmatrix}$$

Crosswind up:
$$\begin{bmatrix} u^n & u^n & u^n \\ u^n & u^{n+1} & u^{n+1} \\ u^{n+1} & u^{n+1} & u^{n+1} \end{bmatrix} \qquad \begin{bmatrix} u^n & u^n & u^{n+1} \\ u^n & u^{n+1} & u^{n+1} \\ u^n & u^{n+1} & u^{n+1} \end{bmatrix}$$

Crosswind down:
$$\begin{bmatrix} u^{n+1} & u^{n+1} & u^{n+1} \\ u^{n+1} & u^{n+1} & u^n \\ u^n & u^n & u^n \end{bmatrix} \qquad \begin{bmatrix} u^{n+1} & u^{n+1} & u^n \\ u^{n+1} & u^{n+1} & u^n \\ u^{n+1} & u^n & u^n \end{bmatrix}$$

a. i-loop as inner sweep loop. b. j-loop as inner sweep loop.

Fig. 4.1. Relaxation sweep directions, $0 \leqslant \theta \leqslant \dfrac{\pi}{2}$.

To apply smoothing analysis, we introduce: (i) the iteration error

$$\delta_{i,j}^n \equiv u_{i,j}^* - u_{i,j}^n, \tag{4.1}$$

with $u_{i,j}^*$ the converged numerical solution in finite volume i, j, and (ii) the Fourier form

$$\delta_{i,j}^n = D\rho^n e^{\mathrm{i}(\beta_1 i + \beta_2 j)}, \tag{4.2}$$

with D constant, ρ the amplification factor, and $\beta_1 \equiv \omega_1 h$ and $\beta_2 \equiv \omega_2 h$, ω_1 and ω_2 being the error mode in i- and j-direction, respectively. In Figs. 4.2 and 4.3, the smoothing factor ρ_s;

$$\rho_s \equiv \sup | \rho(\beta_1, \beta_2) |, \quad (| \beta_1 |, | \beta_2 |) \in \{[0, \pi] \times [0, \pi] \mid | \beta_1 | \in [\frac{\pi}{2}, \pi] \vee | \beta_2 | \in [\frac{\pi}{2}, \pi]\}, \tag{4.3}$$

is given as a function of θ for scheme (2.3) and scheme (3.9), respectively. As is known, the grid-aligned 1-D upwind scheme (2.3) is insensitive to whether the inner loop is the i-loop or the j-loop (Fig. 4.2). As opposed to this, multi-D upwind scheme (3.9) is sensitive to this (Fig. 4.3). Comparing Figs. 4.2 and 4.3, the multi-D scheme appears to have good smoothing properties.

Because such good smoothing properties are not found for zero-crosswind diffusion scheme (3.21a)-(3.21b), for that scheme we study in the following section the convergence properties of defect correction iteration with multi-D upwind scheme (3.9) as the approximate scheme in the inner multigrid iteration. For comparison, a similar study is also made with 1-D upwind scheme (2.3) as the approximate scheme.
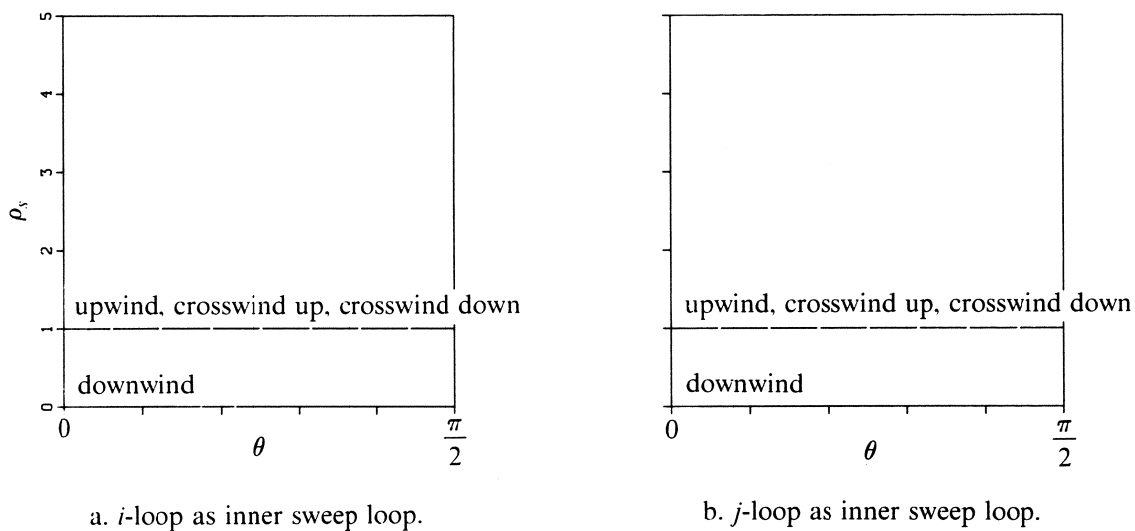
19

a. i-loop as inner sweep loop.

b. j-loop as inner sweep loop.

Fig. 4.2. Smoothing factors point Gauss-Seidel relaxation,
first-order, grid-aligned 1-D upwind scheme (2.3).

a. i-loop as inner sweep loop.
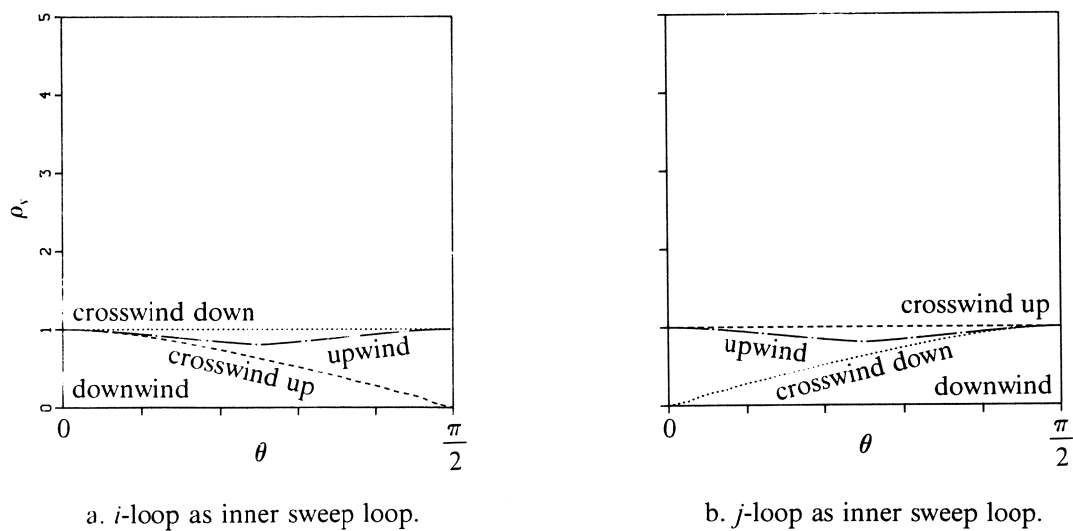

b. j-loop as inner sweep loop.

Fig. 4.3. Smoothing factors point Gauss-Seidel relaxation,
continuously differentiable scheme (3.9).

20

4.2 Convergence of defect correction iteration

Denoting the zero-crosswind diffusion operator by L_h, defect correction iteration reads

$$\tilde{L}_h(u_h^{n+1}) = \tilde{L}_h(u_h^n) - L_h(u_h^n), \quad n = 0, 1, \ldots, N, \tag{4.4}$$

with $\tilde{L}_h$ denoting the positive ('working horse') operator to be inverted. From (4.4) it is clear that the closer the resemblance between the target operator L_h and the approximate operator $\tilde{L}_h$, the better the convergence of the defect correction iteration. Hence, with multi-D upwind scheme (3.9) as the approximate scheme, we expect a better convergence than with 1-D upwind scheme (2.3) as the approximate scheme. Introducing, as before, the iteration error (4.1) in its Fourier form (4.2), we can write for the amplification factor

$$\rho(\beta_1, \beta_2) = 1 - \tilde{L}_h^{-1}(\beta_1, \beta_2) L_h(\beta_1, \beta_2). \tag{4.5}$$

In Fig. 4.4, for each of the two approximate schemes (2.3) and (3.9), and for successively $\theta = 0.1\pi, 0.2\pi, 0.3\pi$ and 0.4π, we give the distributions of the convergence factor ρ_c;

$$\rho_c \equiv |\rho(\beta_1, \beta_2)|, \quad (|\beta_1|, |\beta_2|) \in \{[0, \pi] \times [0, \pi]\}. \tag{4.6}$$

The dashed iso-lines in Fig. 4.4 correspond with $\rho_c = 0.5$. It appears that, for all four values of θ considered, multi-D scheme (3.9) as the approximate scheme gives indeed better convergence factor distributions than 1-D scheme (2.3).

5 Multi-D upwind schemes for the Euler equations

An important difference between model equation (2.1a) and the Euler equations is that for the latter, θ is no longer a constant and not even a scalar. For smooth, steady, 2-D, fully supersonic Euler flows, in each point three characteristic directions exist: the flow angle and the two Mach angles. In shock points, the shock wave angle replaces both Mach angles. For the Euler equations, in the present multi-D upwind schemes, per cell face we determine and use a single rotation angle only. Its determination is discussed in the following section. Here we first discuss its use. The two favorite schemes from the foregoing are generalized to the 2-D Euler equations. The extension is straightforward. Because in the model equation the characteristic information was coming from the left, for the Eulerian numerical flux function, the left cell face states are computed in the same way as the cell face states for the model equation. For the right cell face states, we simply take the point symmetric counterpart of the left states. In this way, in case of all characteristic information coming from the right (supersonic flow from the right), we also have the proper discretization.

5.1 The continuously differentiable scheme

For the left cell face states to be substituted into the Eulerian numerical flux function, continuously differentiable scheme (3.9) as derived for model equation (2.1a)-(2.1b), is applied as

$$\begin{pmatrix} q_{i+\frac{1}{2},j} \\ q_{i,j+\frac{1}{2}} \end{pmatrix}^l = \frac{1}{1 + \tan\theta} \begin{pmatrix} (1 + \frac{1}{2}\tan\theta)q_{i,j} + \frac{1}{2}\tan\theta q_{i,j-1} \\ (\frac{1}{2} + \tan\theta)q_{i,j} + \frac{1}{2}q_{i-1,j} \end{pmatrix}, \quad 0 \le \theta \le \frac{\pi}{2}, \tag{5.1}$$

and for the right cell face states it is applied as

$$\begin{pmatrix} q_{i+\frac{1}{2},j} \\ q_{i,j+\frac{1}{2}} \end{pmatrix}^r = \frac{1}{1 + \tan\theta} \begin{pmatrix} (1 + \frac{1}{2}\tan\theta)q_{i+1,j} + \frac{1}{2}\tan\theta q_{i+1,j+1} \\ (\frac{1}{2} + \tan\theta)q_{i,j+1} + \frac{1}{2}q_{i+1,j+1} \end{pmatrix}, \quad 0 \le \theta \le \frac{\pi}{2}. \tag{5.2}$$

$\theta = 0.1\pi$:

$\theta = 0.2\pi$:

$\theta = 0.3\pi$:

$\theta = 0.4\pi$:

a. 1-D upwind scheme (2.3) as approximate scheme.

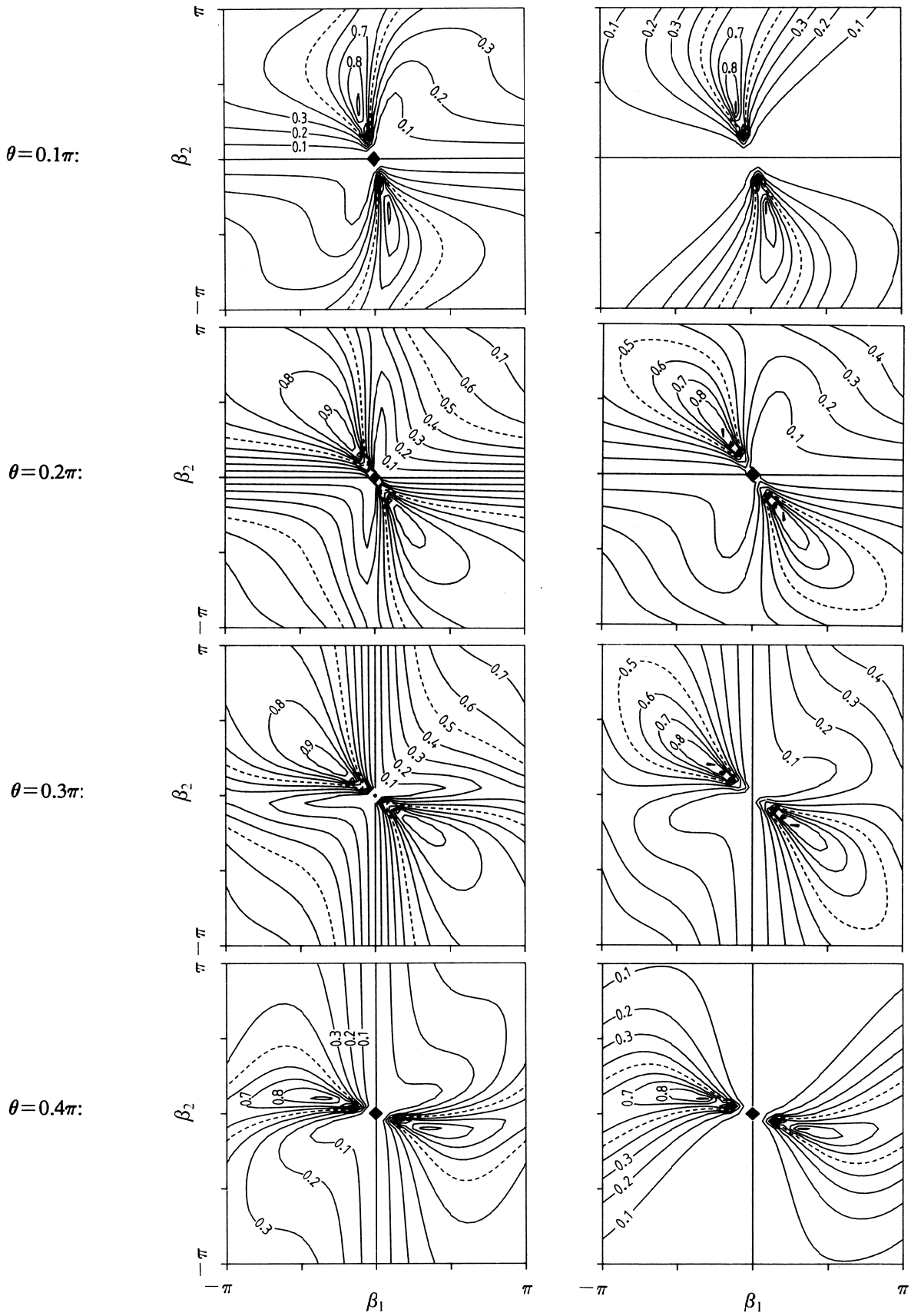b. Multi-D upwind scheme (3.9) as approximate scheme.

Fig. 4.4. Convergence factor distributions defect correction iteration, zero-crosswind diffusion scheme (3.21a)-(3.21b) as target scheme.

22

5.2 The zero-crosswind diffusion scheme

Zero-crosswind diffusion scheme (3.21a)-(3.21b) as derived for model equation (2.1a)-(2.1b) is applied to the Euler equations as

$$
\begin{pmatrix} q_{i+\frac{1}{2},j} \\ q_{i,j+\frac{1}{2}} \end{pmatrix}^l = \begin{pmatrix} q_{i,j} \\ \frac{1}{2}(1+\tan\theta)q_{i-1,j} + \frac{1}{2}(1-\tan\theta)q_{i-1,j+1} \end{pmatrix}, \quad 0 \le \theta \le \frac{\pi}{4}, \tag{5.3a}
$$

$$
\begin{pmatrix} q_{i+\frac{1}{2},j} \\ q_{i,j+\frac{1}{2}} \end{pmatrix}^l = \begin{pmatrix} \frac{1}{2}(1+\frac{1}{\tan\theta})q_{i,j-1} + \frac{1}{2}(1-\frac{1}{\tan\theta})q_{i+1,j-1} \\ q_{i,j} \end{pmatrix}, \quad \frac{\pi}{4} \le \theta \le \frac{\pi}{2}, \tag{5.3b}
$$

and

$$
\begin{pmatrix} q_{i+\frac{1}{2},j} \\ q_{i,j+\frac{1}{2}} \end{pmatrix}^r = \begin{pmatrix} q_{i+1,j} \\ \frac{1}{2}(1+\tan\theta)q_{i+1,j+1} + \frac{1}{2}(1-\tan\theta)q_{i+1,j} \end{pmatrix}, \quad 0 \le \theta \le \frac{\pi}{4}, \tag{5.4a}
$$

$$
\begin{pmatrix} q_{i+\frac{1}{2},j} \\ q_{i,j+\frac{1}{2}} \end{pmatrix}^r = \begin{pmatrix} \frac{1}{2}(1+\frac{1}{\tan\theta})q_{i+1,j+1} + \frac{1}{2}(1-\frac{1}{\tan\theta})q_{i,j+1} \\ q_{i,j+1} \end{pmatrix}, \quad \frac{\pi}{4} \le \theta \le \frac{\pi}{2}. \tag{5.4b}
$$

6 Determination of the rotation angle for the Euler equations

With the present multi-D upwind approach, per cell face we have to select a single rotation θ from the local, multi-D solution. In the following two subsections we consider successively: (i) a technique which looks at all cell faces for *both* the local flow angle *and* a local shock wave angle, and (ii) a technique which looks at all cell faces at *either* the local flow angle only *or* a local shock wave angle only. The first technique, which has been briefly discussed in [22] already, considers per cell face a set of jump relations, e.g. the full set of Rankine-Hugoniot conditions. The latter technique, which is novel, considers the wave path in state space.

6.1 Through jump relations

Suppose that the s-axis as indicated in Fig. 2.1 coincides with an Euler flow discontinuity. Denoting the local flow states at the left and right side of the discontinuity by q^l and q^r, respectively, satisfaction of the full set of Rankine-Hugoniot conditions (across the discontinuity) implies

$$
f(q^l)\sin\theta - g(q^l)\cos\theta = f(q^r)\sin\theta - g(q^r)\cos\theta, \tag{6.1a}
$$

$$
f(q) = \begin{pmatrix} \rho u \\ \rho u^2 + p \\ \rho u v \\ \rho u(e + \frac{p}{\rho}) \end{pmatrix}, \quad g(q) = \begin{pmatrix} \rho v \\ \rho v u \\ \rho v^2 + p \\ \rho v(e + \frac{p}{\rho}) \end{pmatrix}, \tag{6.1b}
$$

with for a perfect gas: $e = \frac{1}{\gamma-1}\frac{p}{\rho} + \frac{1}{2}(u^2 + v^2)$. In a general discrete case, it may well be that (6.1a) is not satisfied for any $\theta \in [0, 2\pi]$; i.e.

$$
\big(f(q^l) - f(q^r)\big)\sin\theta - \big(g(q^l) - g(q^r)\big)\cos\theta = r(\theta) \ne 0, \quad \forall\, \theta \in [0, 2\pi]. \tag{6.2}
$$

A proper angle θ is found by minimizing a norm of the error vector $r(\theta)$. Taking the Euclidian norm, minimization by the least squares method is straightforward; it yields

$$
r \cdot \frac{dr}{d\theta} = 0, \tag{6.3}
$$

or, with (6.2), assuming q^l and q^r to be functions of θ as well:

$$\left[\big(f(q^l) - f(q^r)\big) \sin\theta - \big(g(q^l) - g(q^r)\big) \cos\theta\right] \cdot$$

$$\left[\left(\frac{df(q^l)}{dq}\frac{dq^l}{d\theta} - \frac{df(q^r)}{dq}\frac{dq^r}{d\theta}\right) \sin\theta + \big(f(q^l) - f(q^r)\big) \cos\theta\right.$$

$$\left. - \left(\frac{dg(q^l)}{dq}\frac{dq^l}{d\theta} - \frac{dg(q^r)}{dq}\frac{dq^r}{d\theta}\right) \cos\theta + \big(g(q^l) - g(q^r)\big) \sin\theta\right] = 0. \qquad (6.4)$$

The computation of θ from (6.4) requires the iterative solution of a nonlinear equation of the form $A(\theta)\cos^2\theta + B(\theta)\cos\theta\sin\theta + C(\theta)\sin^2\theta = 0$, where the evaluation of the coefficients $A(\theta)$, $B(\theta)$ and $C(\theta)$ requires the computation of Jacobian matrices. Neglecting for simplicity the θ-dependence of q^l and q^r, instead of (6.4), we find

$$\left[\big(f(q^l) - f(q^r)\big) \sin\theta - \big(g(q^l) - g(q^r)\big) \cos\theta\right] \cdot$$
$$\left[\big(f(q^l) - f(q^r)\big) \cos\theta + \big(g(q^l) - g(q^r)\big) \sin\theta\right] = 0, \qquad (6.5)$$

which directly yields as expression for θ

$$\frac{1}{2}\tan 2\theta = \frac{\big(f(q^l) - f(q^r)\big) \cdot \big(g(q^l) - g(q^r)\big)}{\big(f(q^l) - f(q^r)\big) \cdot \big(f(q^l) - f(q^r)\big) - \big(g(q^l) - g(q^r)\big) \cdot \big(g(q^l) - g(q^r)\big)}. \qquad (6.6)$$

To further simplify the technique, instead of the full set of Rankine-Hugoniot conditions, only some subset may be considered.

A property of the present jump relations approach is that if both a contact discontinuity and a shock wave occur at a cell face, the value of θ found by minimizing $r(\theta)$ is not necessarily that which corresponds with the most dominant of both discontinuities. Given the rareness of this common occurrence of a contact discontinuity and shock wave, in practice this property is not of too great weight. Another property is that no unique value of θ is found from (6.6) if $q^l = q^r$. In this case, (6.1a) is satisfied for any value of θ. Of course, a repair for this is easily made.

6.2 Through wave path in state space

Besides for the computation of the numerical flux, at each cell face, the wave path in state space can also be used for computing the rotation angle θ. As the wave path we consider the one of the P-variant of Osher's scheme [10]. For the steady 2-D Euler equations and a perfect gas, with $c \equiv \sqrt{\gamma\frac{p}{\rho}}$, $z \equiv \ln\left(\frac{p}{\rho^\gamma}\right)$, the P-variant's wave path is shown in Fig. 6.1.
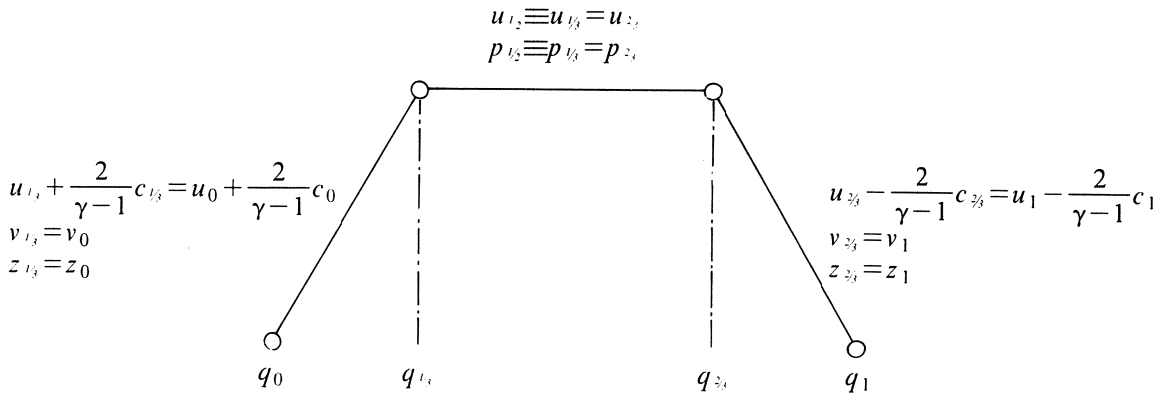

Fig. 6.1. Wave path in state space according to P-variant Osher scheme (perfect gas).

24

For the determination of the angle θ, the states $q_0 \equiv (u_0, v_0, c_0, z_0)^T$ and $q_1 \equiv (u_1, v_1, c_1, z_1)^T$ are taken dependent on θ as

$$q_0(\theta) = T(\theta)q^l, \quad q_1(\theta) = T(\theta)q^r, \qquad (6.7a)$$

with

$$T(\theta) = \begin{pmatrix} \cos\theta & \sin\theta & 0 & 0 \\ -\sin\theta & \cos\theta & 0 & 0 \\ 0 & 0 & 1 & 0 \\ 0 & 0 & 0 & 1 \end{pmatrix}, \qquad (6.7b)$$

and with the states q^l and q^r in (6.7a) given. At the cell faces $i+\frac{1}{2}, j$ and $i, j+\frac{1}{2}$, for q^l and q^r we take e.g.

$$\begin{pmatrix} q_{i+\frac{1}{2},j} \\ q_{i,j+\frac{1}{2}} \end{pmatrix}^l = \begin{pmatrix} q_{i,j} \\ q_{i,j} \end{pmatrix}, \qquad (6.8a)$$

$$\begin{pmatrix} q_{i+\frac{1}{2},j} \\ q_{i,j+\frac{1}{2}} \end{pmatrix}^r = \begin{pmatrix} q_{i+1,j} \\ q_{i,j+1} \end{pmatrix}. \qquad (6.8b)$$

Then, a suitable rotation angle can be found by maximizing one of the two Riemann invariants along the middle subpath of the P-variant's wave path in state space. We maximize either the invariant velocity component

$$u_{\frac{1}{2}}(\theta) = \frac{1}{1+\alpha}\left[\left(u_1(\theta) - \frac{2}{\gamma-1}c_1\right) + \alpha\left(u_0(\theta) + \frac{2}{\gamma-1}c_0\right)\right], \qquad (6.9a)$$

or the invariant pressure

$$p_{\frac{1}{2}}(\theta) = \left[\frac{\gamma-1}{2(1+\alpha)\sqrt{\gamma e^{\frac{z_0}{\gamma}}}}\left(u_0(\theta) - u_1(\theta) + \frac{2}{\gamma-1}(c_0+c_1)\right)\right]^{\frac{2\gamma}{\gamma-1}}, \qquad (6.9b)$$

where in both: $\alpha \equiv e^{\frac{z_1-z_0}{2\gamma}}$.

Theorem 6.1
For the P-variant's wave path in state space, the orientation of a contact discontinuity follows from the maximization of the velocity component $u_{\frac{1}{2}}(\theta)$.

Proof
From (6.9a), it follows with (6.7a)-(6.7b):

$$\frac{du_{\frac{1}{2}}}{d\theta} = \frac{1}{1+\alpha}\left[-\sin\theta\, u^r + \cos\theta\, v^r + \alpha(-\sin\theta\, u^l + \cos\theta\, v^l)\right]. \qquad (6.10)$$

From (6.10), we derive that $u_{\frac{1}{2}}$ is maximal for

$$\tan\theta = \frac{\alpha v^l + v^r}{\alpha u^l + u^r}, \qquad (6.11)$$

which is a biased relation for the orientation of a contact discontinuity. $\square$

Remark 6.1
For the isentropic case $\alpha = 1$, (6.11) simplifies to the known centered relation

$$\tan\theta = \frac{v^l + v^r}{u^l + u^r}. \qquad (6.12)$$

25

Remark 6.2

The physical meaning of (6.11) for $\alpha \neq 1$ can be explained for the isobaric case $p^l = p^r$. For this case, (6.11) simplifies to the (still biased) relation

$$\tan \theta = \frac{\sqrt{\rho^l}\, v^l + \sqrt{\rho^r}\, v^r}{\sqrt{\rho^l}\, u^l + \sqrt{\rho^r}\, u^r}.$$

(6.13)

From (6.13) it follows that of the two states q^l and q^r, the state with the higher density has a stronger weight in the determination of the angle θ. To our opinion this is physically more proper than the absence of any such weight in the commonly used centered relation (6.12).

Theorem 6.2

For the P-variant's wave path in state space, the orientation of the normal at a shock wave follows from the maximization of the pressure $p_{\frac{1}{2}}(\theta)$.

Proof

From (6.9b), it follows with (6.7a)-(6.7b):

$$\frac{dp_{\frac{1}{2}}}{d\theta} = \frac{1}{1+\alpha} \sqrt{\frac{\gamma p_{\frac{1}{2}}^{\frac{\gamma+1}{\gamma}}}{e^{\frac{z_0}{\gamma}}}}\; \left(-\sin\theta (u^l - u^r) + \cos\theta (v^l - v^r) \right).$$

(6.14)

From (6.14), we derive that $p_{\frac{1}{2}}$ is maximal for

$$\tan \theta_n = \frac{v^l - v^r}{u^l - u^r}.$$

(6.15)

This is a relation for the orientation of the normal at a shock wave, because - given the θ-independence of p_0 and p_1 - the maximization of $p_{\frac{1}{2}}$ is identical to the maximization of either $p_{\frac{1}{2}} - p_0$ or $p_{\frac{1}{2}} - p_1$; the underlying, natural quantities for finding the orientation of the normal at a shock wave. □

Corollary

The shock wave angle itself, i.e. the rotation angle θ, satisfies

$$\tan \theta = \frac{u^l - u^r}{v^r - v^l}.$$

(6.16)

Remark 6.3

In contrast with (6.11), the result (6.16) is known. It directly follows from the jump relation which states that the tangential velocity components at the up- and downstream side of a shock wave are equal.

Remark 6.4

As opposed to (6.11), (6.16) contains differences, which makes it sensitive to noise and non-uniqueness. In principle, as a remedy against this, a blended formula like that proposed in [24], can also be constructed on the basis of (6.11) and (6.16).

Remark 6.5

Notice that by taking the shock wave angle as rotation angle, the upwinding is not done normal to the shock wave, cf. e.g. Davis [3], but - instead - along the shock wave; i.e. along the (merged) characteristics.

7 Numerical results

To investigate the theoretical results found in the previous sections, in this section - for a perfect gas with $\gamma = 1.4$ - we perform numerical experiments for successively: (i) four supersonic Euler flows with oblique contact discontinuity (Fig. 7.1a, notice that the discontinuity has both a velocity and a temperature jump), and (ii) two supersonic Euler flows with an oblique shock wave (Fig. 7.1b). The flow with the contact discontinuity is considered for the flow angles $\theta = 0.1\pi, 0.2\pi, 0.3\pi$ and 0.4π, the flow with shock wave is considered for the shock wave angles $\theta = \frac{\pi}{4}$ and $\theta = \frac{\pi}{8}$. (Notice that the inflow Mach numbers corresponding with both shock wave cases are different; $M^L = 2$ and $M^L = 4$, respectively.) All flows are computed on the 32×32-grid given in Fig. 7.2. In all cases - for simplicity - at each of the four boundaries, the exact solution is imposed (overspecification). In all cases, the problem is solved by a multigrid method for which the coarsest grid is a 2×2-grid. The multigrid method is nonlinear multigrid (FAS) with V-cycles, and with a single pre- and post-relaxation sweep per level. For a detailed description of the nonlinear multigrid method, we refer to [9]. Notice that with novel scheme (5.1)-(5.2) to be locally linearized in the inner multigrid iteration, we also have new 4×4 derivative matrices. Since we apply exact Newton iteration, these matrices contain contributions which originate from the solution-dependent rotation angle. In all cases we take as the initial solution: the solution with $q = q^L$ (the exact q^L's from Figs. 7.1a and 7.1b) uniformly constant over the complete domain.

a. Oblique contact discontinuity
$(\theta = 0.1\pi, 0.2\pi, 0.3\pi, 0.4\pi, p = 1)$.

b. Oblique shock wave
$(\theta = \frac{\pi}{4}, M^L = 2$ and $\theta = \frac{\pi}{8}, M^L = 4)$.
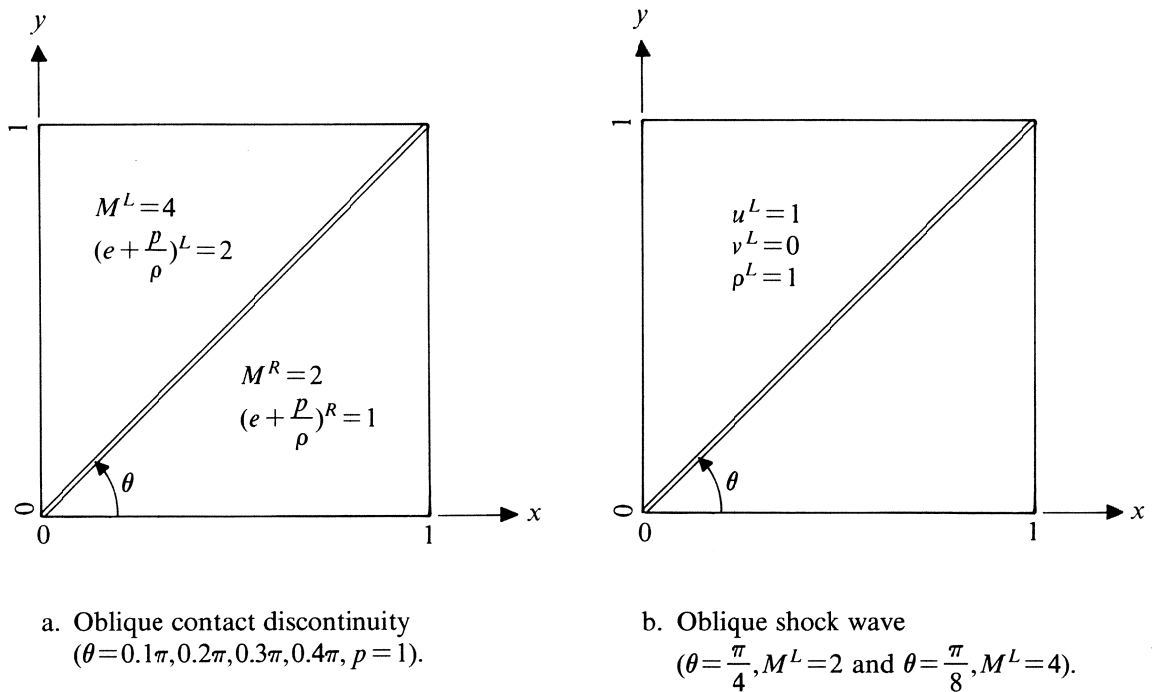
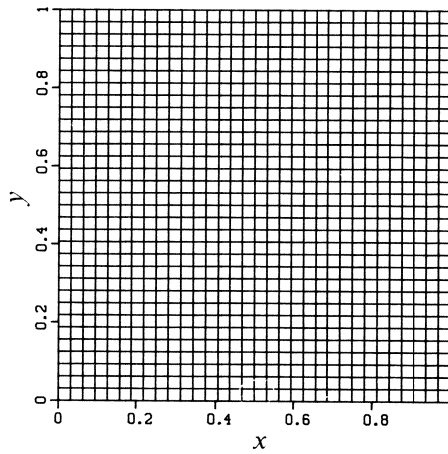Fig. 7.1. Test cases to be considered on unit square.

Fig. 7.2. Finest grid (32×32) to be considered for all cases.

7.1 Flows with contact discontinuity

7.1.1 Reference results

In Fig. 7.3 we first give reference solutions for the present four test cases. In each of the three graphs in Fig. 7.3, we plotted on top of each other: the enthalpy $(e + \frac{p}{\rho})$ distributions for $\theta = 0.1\pi, 0.2\pi, 0.3\pi$ and 0.4π. The iso-enthalpy values considered in these and all following enthalpy distributions are: $1.1, 1.2, 1.3, \ldots, 1.9$. Because of the severe smearing of the first-order, grid-aligned 1-D upwind scheme, in the corresponding graph (Fig. 7.3b) hardly any distinction can be made between these four solutions. Notice that the layers along $x = 1$ and $y = 1$ in Fig. 7.3b and Fig. 7.3c (and also in the following enthalpy graphs), are only due to the overspecification.

The convergence histories corresponding with the main reference scheme (the first-order, grid-aligned 1-D upwind scheme), are given in Fig. 7.4.

a. Discrete exact.

b. First-order, grid-aligned 1-D upwind scheme.

c. Higher-order, grid-aligned 1-D upwind scheme ($\kappa = \frac{1}{3}$).
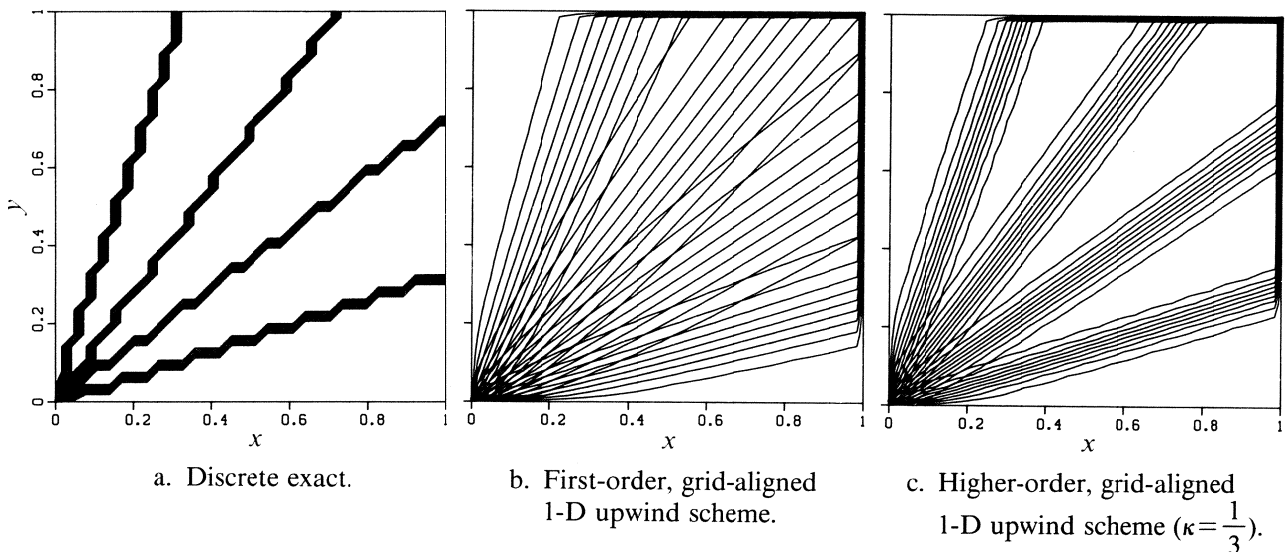
Fig. 7.3. Reference enthalpy distributions.

28
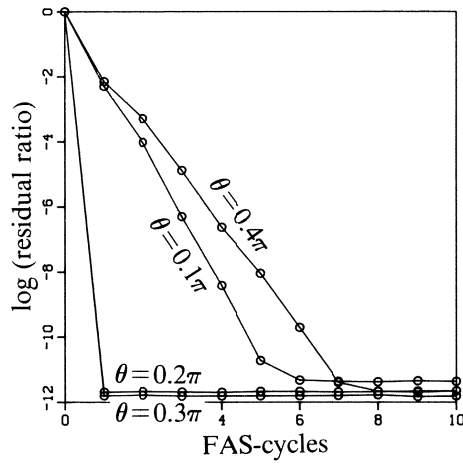
Fig. 7.4. Reference multigrid convergence histories,
first-order, grid-aligned 1-D upwind scheme.

7.1.2 Results continuously differentiable scheme

In Fig. 7.5 we give results obtained by multi-D scheme (5.1)-(5.2), with the local flow angle according to (6.11) as the rotation angle. Though more accurate than the first-order reference distributions in Fig. 7.3b, the enthalpy distributions (Fig. 7.5a) are still insufficiently accurate. Though not as very fast as the reference convergence in Fig. 7.4, the present scheme's multigrid convergence (Fig. 7.5b) is still adequate.
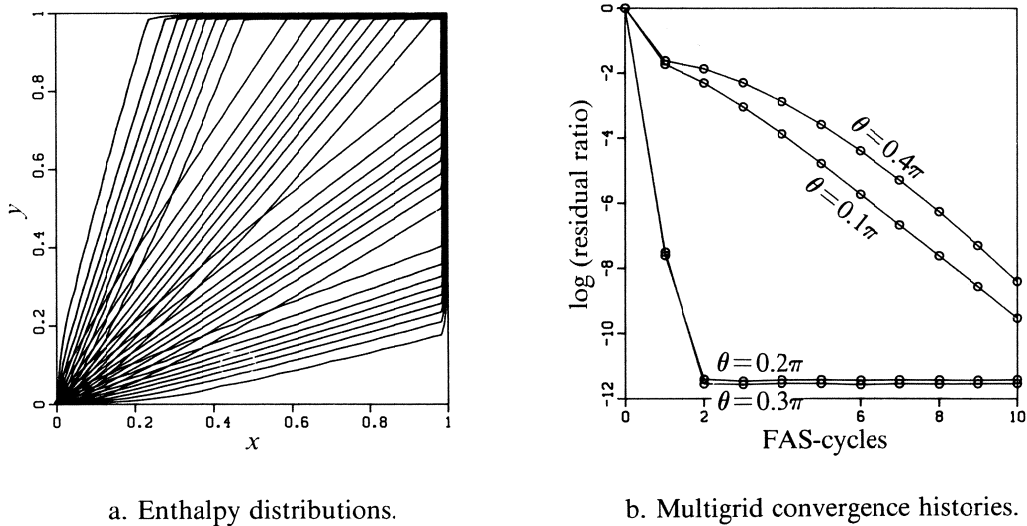
a. Enthalpy distributions.

b. Multigrid convergence histories.

Fig. 7.5. Results continuously differentiable scheme (5.1)-(5.2).

7.1.3 Results zero-crosswind diffusion scheme

In Fig. 7.6 we give the enthalpy distributions for the zero-crosswind diffusion scheme (5.3a)-(5.4b) as obtained after 10 defect correction cycles (with a single nonlinear multigrid cycle per defect correction cycle), and with (6.11) for the angle considered at each cell face. All enthalpy distributions in Fig. 7.6 appear to be even less diffused than those of the $\kappa = \frac{1}{3}$-scheme (Fig. 7.3c). (Almost in agreement with theory, the distributions appear to be almost free of crosswind diffusion.) Although in principle the non-positivity of the scheme allows solutions with spurious oscillations, the distributions in Fig. 7.6 are still monotone. (Probably, the specific flow problems considered here do not easily lead to oscillations; to obtain the monotone $\kappa = \frac{1}{3}$-solutions given in Fig. 7.3c, a limiter did not need to be applied either.)

An impression of the convergence rate of the defect correction iteration is given in Fig. 7.7. The distributions in Fig. 7.7a are those of the starting solutions of the defect correction iteration, i.e. the solutions of continuously differentiable scheme (5.1)-(5.2) after a single multigrid cycle. (Notice, as a side-result, the perfect agreement already between these early distributions and those as found after 10 multigrid cycles (Fig. 7.5a)). We observe that the convergence of the defect correction iteration is fast.
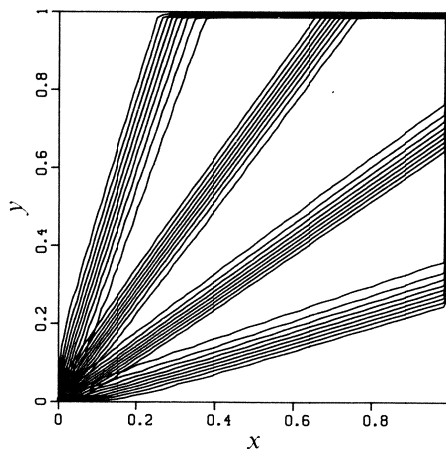

Fig. 7.6. Enthalpy distributions zero-crosswind diffusion scheme (5.3a)-(5.4b), after *10th* defect correction cycle.
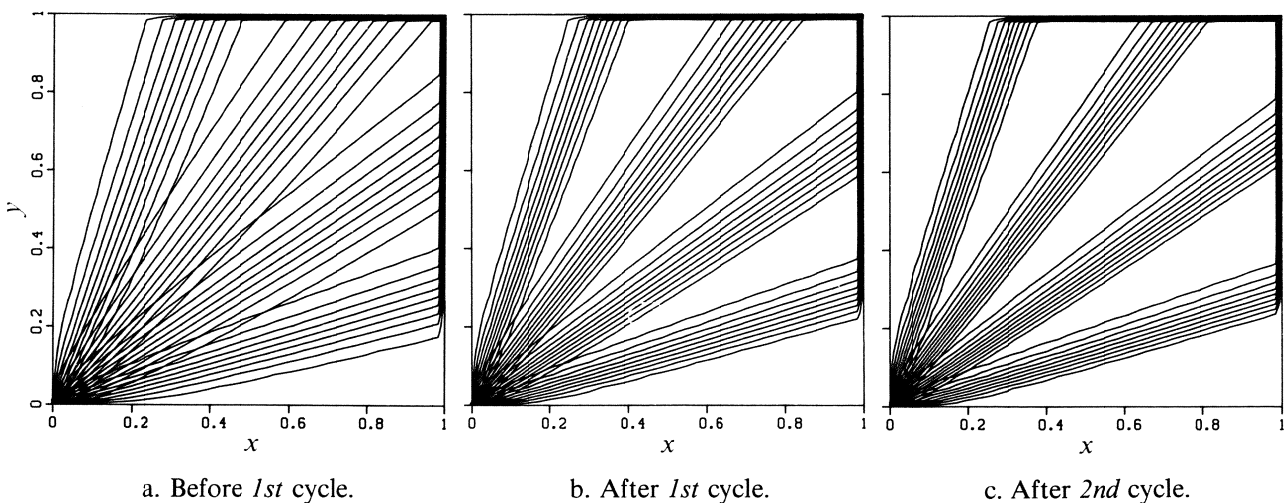

a. Before *1st* cycle. b. After *1st* cycle. c. After *2nd* cycle.

Fig. 7.7. Convergence histories defect correction iteration, enthalpy distributions zero-crosswind diffusion scheme (5.3a)-(5.4b).

7.2 Flows with shock wave

7.2.1 Reference results

As for the flows with contact discontinuity, we first give reference results. Now we give Mach number distributions (Fig. 7.8). Here solutions are also plotted on top of each other. The iso-Mach number values shown are: (i) $1.50, 1.55, 1.60, \ldots, 1.95$ for the case with $\theta = \frac{\pi}{4}, M^L = 2$, and (ii) $3.30, 3.35, 3.40, \ldots, 3.95$ for the case with $\theta = \frac{\pi}{8}, M^L = 4$. Similar to the flows with contact discontinuity, the layer along $x = 1$ is caused by the overspecification. The higher-order discretization applied for obtaining the reference results given in Fig. 7.8c deviates from the one applied for Fig. 7.3c in that here a limiter is invoked to guarantee a monotonous solution (the $\kappa = \frac{1}{3}$-limiter derived in [18]). The distributions shown in Fig. 7.8c are obtained after two defect correction cycles.

| a. Discrete exact. | b. First-order, grid-aligned 1D upwind. | c. Higher-order, grid-aligned 1-D upwind (limited $\kappa = \frac{1}{3}$). |
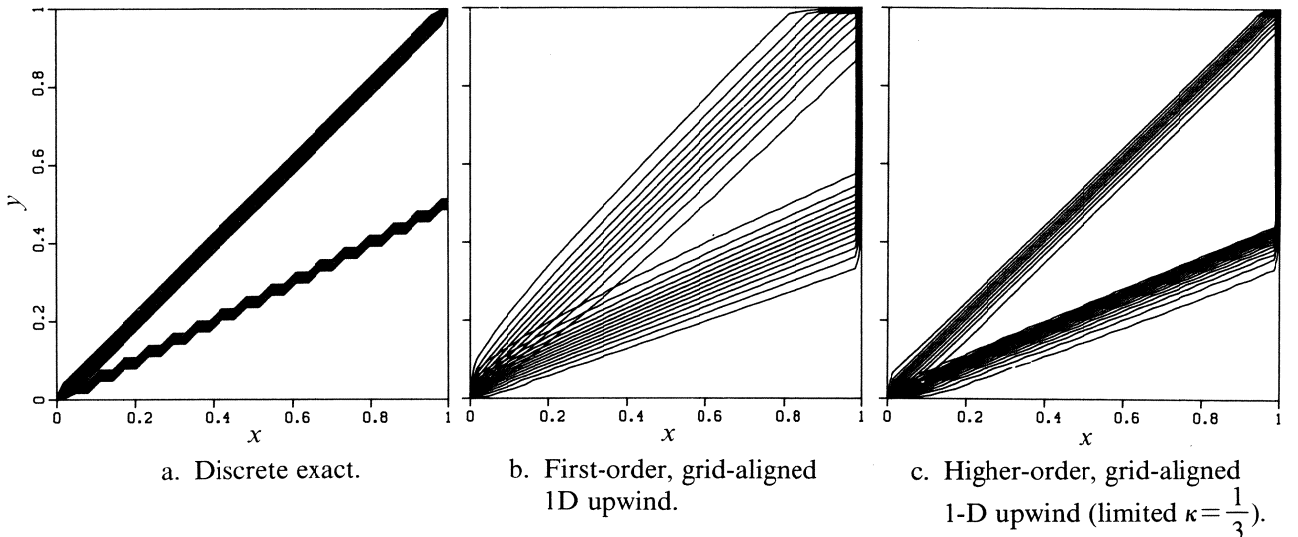
Fig. 7.8. Reference Mach number distributions.

7.2.2 Results zero-crosswind diffusion scheme

The Mach number distributions obtained after two defect correction cycles with zero-crosswind diffusion scheme (5.3a)-(5.4b) are given in Fig. 7.9. The rotation angle considered here is the shock wave angle according to (6.16). To avoid difficulties in the uniform flow parts, in our actual computations, in addition to (6.16), we applied the following threshold relations. If at a cell face we had both $| v^l - v^r | > 0.01 | v^L - v^R |$ and $| u^l - u^r | > 0.01 | u^L - u^R |$, with the superscript pairs l, r and L, R referring to respectively the numerical and exact pre- and post-shock flow (Fig. 7.1b), then (6.16) was applied. Otherwise, at that cell face we simply applied the first-order, grid-aligned 1-D upwind scheme; i.e. $\theta = 0$ at vertical cell faces and $\theta = \frac{\pi}{2}$ at horizontal cell faces. A difficulty of the present shock problems in comparison with the previous contact problems is that the local rotation angles in the initial solutions are not equal to those of the converged solutions. To ensure sufficient robustness, instead of multi-D upwind scheme (5.1)-(5.2), we had to apply the standard first-order, grid-aligned 1-D upwind scheme as the approximate scheme in the inner nonlinear multigrid iteration. From Fig. 7.9 it appears that after two defect correction cycles, the solution seems to be free of crosswind diffusion, but for $\theta = \frac{\pi}{4}$ it has become non-monotone. Given the good accuracy, construction of a compact multi-D limiter might be useful. The monotonicity preserved at $\theta = \frac{\pi}{8}$ suggests that an appropriate limiter might be dependent on the rotation angle.
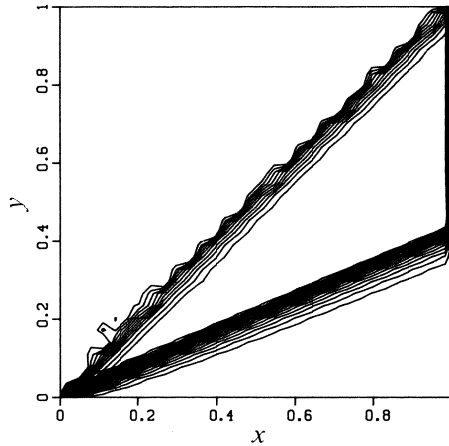
31

Fig. 7.9. Mach number distributions after *2nd* defect correction cycle,
zero-crosswind diffusion scheme (5.3a)-(5.4b).

8 Conclusions

In the present paper, we analyzed and tested the accuracy and solvability properties of some simple multi-D upwind schemes. Two interesting multi-D upwind schemes have been derived: (i) a positive, continuously differentiable scheme and (ii) a non-positive, zero-crosswind diffusion scheme. Both schemes are based on a 1-D Riemann solver. Their multi-D nature is realized through a local, solution-dependent rotation of the left and right Riemann state, which allows us to keep the number of numerical flux computations per cell face equal to one. Good efficiency can be attained by means of nonlinear multigrid iteration and defect correction iteration. The accuracy and efficiency of the numerical results are promising. One important result is that for flows with contact discontinuities, the performance of nonlinear multigrid with point Gauss-Seidel relaxation is very good when one applies the positive, continuously differentiable scheme. Another important result is that, also for flows with contact discontinuities, the solutions obtained with the zero-crosswind diffusion scheme, are even less diffused than those obtained with the grid-aligned $\kappa = \frac{1}{3}$-scheme; they appear to be nearly free of any crosswind diffusion. Moreover, their computation by means of defect correction iteration (with the positive, continuously differentiable scheme as the approximate scheme) is efficient. The zero-crosswind diffusion scheme seems to be well-suited for a very accurate computation of e.g. vortex flows.

References

[1] M.J. BAINES, University of Reading, Numerical Analysis Report 10/83, 1983 (unpublished).

[2] L.A. CATALANO AND H. DECONINCK, Von Karman Institute for Fluid Dynamics, Technical Note 173, 1990 (unpublished).

[3] S.F. DAVIS, *J. Comput. Phys.*, **56**, 65 (1984).

[4] J.-A. DESIDERI AND P.W. HEMKER, Center for Mathematics and Computer Science, Report NM-R9004, 1990 (unpublished).

[5] E. DICK, in *Lecture Notes in Pure and Applied Mathematics,* Vol.110, edited by S.F. Mc-Cormick (Dekker, New York, 1988).

[6] W. HACKBUSCH, *Multi-Grid Methods and Applications* (Springer, Berlin, 1985).

[7] P.W. HEMKER, in *Lecture Notes in Mathematics,* Vol.1228, edited by W. Hackbusch *et al.* (Springer, Berlin, 1986).

[8] P.W. HEMKER AND B. KOREN, in *Notes on Numerical Fluid Mechanics,* Vol.26, edited by A. Dervieux *et al.* (Vieweg, Braunschweig, 1989).

[9] P.W. HEMKER AND B. KOREN, in *Advances in Computational Fluid Dynamics,* edited by W.G. Habashi *et al.* (to appear).

[10] P.W. HEMKER AND S.P. SPEKREIJSE, *Appl. Numer. Math.,* **2**, 475 (1986).

[11] CH. HIRSCH, C. LACOR AND H. DECONINCK, *AIAA Paper 87-1163* (1987).

[12] CH. HIRSCH AND C. LACOR, *AIAA Paper 89-1958* (1989).

[13] A. JAMESON, *Comm. Pure Appl. Math.,* **27**, 283 (1974).

[14] A. JAMESON, W. SCHMIDT AND E. TURKEL, *AIAA Paper 81-1259* (1981).

[15] D.C. JESPERSEN, *Appl. Math. Comput.,* **13**, 357 (1983).

[16] B. KOREN, *J. Comput. Phys.,* **77**, 183 (1988).

[17] B. KOREN, *J. Comput. Phys.,* **87**, 25 (1990).

[18] B. KOREN, *Int. J. Numer. Meth. Fluids,* **11**, 99 (1990).

[19] D. KRÖNER, in *Notes on Numerical Fluid Mechanics,* Vol.24, edited by J. Ballmann *et al.* (Vieweg, Braunschweig, 1989).

[20] W. LAYTON, *J. Comput. Phys.,* **90**, 336, (1990).

[21] B. VAN LEER, in *Lectures in Applied Mathematics,* Vol.22, edited by B.E. Engquist *et al.* (Amer. Math. Soc., Providence, RI, 1985).

[22] B. VAN LEER, in *Notes on Numerical Fluid Mechanics,* Vol.26, edited by A. Dervieux *et al.* (Vieweg, Braunschweig, 1989).

[23] R.J. LEVEQUE, *J. Comput. Phys.,* **78**, 36 (1988).

[24] D.W. LEVY, K.G. POWELL AND B. VAN LEER, *AIAA Paper 89-1931* (1989).

[25] G. MORETTI, *Computers and Fluids,* **7**, 191 (1979).

[26] E.M. MURMAN AND J.D. COLE, *AIAA J.,* **9**, 114 (1971).

[27] S. OSHER AND F. SOLOMON, *Math. Comput.,* **38**, 339 (1982).

[28] P. DE PALMA, H. DECONINCK AND R. STRUIJS, Von Karman Institute for Fluid Dynamics, Technical Note 172, 1990 (unpublished).

[29] S.V. PATANKAR, *Numerical Heat Transfer and Fluid Flow* (Hemisphere, New York, 1980).

[30] K.G. POWELL AND B. VAN LEER, *AIAA Paper 89-0095* (1989).

[31] G.D. RAITHBY, *Comput. Meth. Appl. Mech. Eng.,* **9**, 75 (1976).

[32] G.D. RAITHBY, *Comput. Meth. Appl. Mech. Eng.,* **9**, 153 (1976).

[33] P.L. ROE, *J. Comput. Phys.,* **63**, 458 (1986).

[34] C.L. RUMSEY, B. VAN LEER AND P.L. ROE, The University of Michigan, Department of Aerospace Engineering, report, 1990 (unpublished).

[35] D. SIDILKOVER, Weizmann Institute of Science, Doctoral Thesis, 1989 (unpublished).

[36] P.K. SMOLARKIEWICZ, *J. Comput. Phys.,* **54**, 325 (1984).

[37] R. STRUIJS AND H. DECONINCK, in *Notes on Numerical Fluid Mechanics,* Vol.29, edited by P. Wesseling (Vieweg, Braunschweig, 1990).

Contents